Cronfa - Swansea University Open Access Repository

_____

This is an author produced version of a paper published in:
International Journal for Numerical Methods in Engineering

_____

Cronfa URL for this paper:

http://cronfa.swan.ac.uk/Record/cronfa39052

_____

Paper:

Bagwell, S., Ledger, P., Gil, A. & Mallett, M. (2018). Transient solutions to non-linear acousto-magneto-mechanical coupling for axisymmetric MRI scanner design. _International Journal for Numerical Methods in Engineering_

http://dx.doi.org/10.1002/nme.5802

_____

RESEARCH ARTICLE

Transient solutions to nonlinear acousto-magneto-mechanical coupling for axisymmetric MRI scanner design

S. Bagwell[1] | P.D. Ledger[1] | A.J. Gil[1] | M. Mallett[2]

[1]Zienkiewicz Centre for Computational Engineering, College of Engineering, Swansea University Bay Campus, Swansea, UK

[2]Siemens Healthcare Ltd., MR Magnet Technology, Witney, Oxon, UK

Correspondence
P.D. Ledger, Zienkiewicz Centre for Computational Engineering, College of Engineering, Swansea University Bay Campus, Swansea SA1 8EN, UK.
Email: p.d.ledger@swansea.ac.uk

Summary

In this work, we simulate the coupled physics describing a magnetic resonance imaging (MRI) scanner by using a higher-order finite element discretisation and a Newton-Raphson algorithm. To apply the latter, a linearisation of the nonlinear system of equations is necessary, and we consider two alternative approaches. In the first approach, ie, the *nonlinear approach*, there is no approximation from a physical standpoint, and the linearisation is performed about the current solution. In the second approach, ie, the *linearised approach*, we realise that the MRI problem can be described by small dynamic fluctuations about a dominant static solution and linearise about the latter. The *linearised approach* permits solutions in the frequency domain and provides a computationally efficient way to solve this challenging problem, as it allows the tangent stiffness matrix to be inverted independently of time or frequency. We focus on transient solutions to the coupled system of equations and address the following two important questions: (i) how good is the agreement between the computationally efficient *linearised approach* compared with the intensive *nonlinear approach* and (ii) over what range of MRI operating conditions can the *linearised approach* be expected to provide acceptable results for outputs of interest in an industrial context for MRI scanner design? We include a set of academic and industrially relevant examples to benchmark and illustrate our approach.

KEYWORDS

acousto-magneto-mechanical coupling, linearisation, MRI scanner, multifield systems, Newton methods, time integration implicit

1 | INTRODUCTION

In recent years, magnetic resonance imaging (MRI) scanners, illustrated in Figure 1, have become an indispensable tool for use in medical imaging. Their capability to nonintrusively diagnose a range of medical ailments, such as tumours,[1] damaged cartilage, fractures,[2] internal bleeding, and even detection of multiple sclerosis[3] make them a desirable imaging

FIGURE 1 Patient on magnetic resonance imaging (MRI) scanner bed with localised torso receiver coils, courtesy of Siemens [Colour figure can be viewed at wileyonlinelibrary.com]

technique for clinical use. The increasing accuracy in MRI has become a topic of particular importance in recent years, due to the need for more accurate diagnosis of medical conditions, such as cancer.[4,5]

Magnetic resonance imaging scanner resolution is determined by the strength of the static magnetic field, ie, $\boldsymbol{H}^{\mathrm{DC}}$, produced by the main magnet. The magnitude of magnetic flux density of such fields, ie, $|\boldsymbol{B}^{\mathrm{DC}}|$, is typically in the region of 1.5 to 3 T (approximately 30 000 to 70 000 times the strength of that of the Earth) for clinical operation,[6-8] with some 7-T units in use for medical research applications.[9,10] Recently, the Siemens 7-T magnet, the MAGNETOM Terra,[11] has also been cleared for clinical use and research use. The magnitude of the magnetic flux density, quoted by manufacturers, is defined as the maximum value of the flux density magnitude on the imaging bore axis,* in the centre where the patient lies, as shown in Figure 1. Recent advances in MRI design have resulted in magnets of flux densities of up to 12 T coming into production, which will allow for very high resolution images to be obtained, compared with the current systems.[12] These scanners all typically utilise superconducting magnets consisting of wound conducting wires resembling solenoids that are supercooled by being immersed in liquid helium (to temperatures of approximately 4°K). Some open C-shaped MRI scanners, which utilise permanent magnets to generate the static field, are still available, but these are less common in current imaging units due to their relatively low flux densities of approximately 0.3 T.

In addition to the static field generated by the main magnet, MRI scanners use pulsed time-varying magnetic field gradients, generated through sets of resistive coils, which excite the tissues and generate images of the patient. The gradient in the magnetic flux density of these fields is much smaller than the flux density of the main static field, typically with amplitudes in the region of 30 to 80×10^{-3} T/m.[6-8,†] In the presence of conducting bodies, these time-varying fields give rise to eddy currents, which exert Lorentz forces in the conductors. These forces generate magnetic stresses in the conducting components, which, in turn, cause them to deform and vibrate. Furthermore, these vibrations generate Lorentz currents, which cause further perturbations in the magnetic field. They also cause the surrounding free-space region of air to perturb, generating acoustic pressure waves, resulting in audible noise that can cause discomfort for the patient. These generated pressure waves can also rebound off other conducting components causing further deformations to the conductors and more acoustic waves to form. This, in turn, creates further perturbations of the magnetic field resulting in a fully coupled transient system of nonlinear transient PDEs comprising the Maxwell, elasticity, and acoustic equations.[13]

With increasing interest in the design of more economical (reduced amount of material, decreased power consumption) and more advanced MRI systems (capable of producing stronger magnetic fields),[14] of late, the prediction of the physical behaviours of such scanners has become an important area of research, in particular, the computational modelling of these systems. As such, an emphasis on the reduction of the computational cost of simulations is of great importance to the medical imaging industry. Many single field attempts to analyse the magnetic field of MRI scanners have been published; finite-difference time-domain methods for the calculation of eddy currents arising from transient gradient coils in MRI scanners,[15-17] with analysis also of the effects on the human body,[18-20] and methods for "fast" analysis and design of the MRI coils.[21,22] A number of works have also been published, which focus on the analysis of superconducting solenoids,[23] as well as the on full MRI scanners [24,25] and consider the structural design of higher field scanners.[26] Acoustic effects in MRI scanners have also been investigated,[27] with attempts to design noise reduction systems[28,29] and even analyse the

---

*The imaging bore is located in free space and as such $\boldsymbol{B}^{\mathrm{DC}} = \mu_0 \boldsymbol{H}^{\mathrm{DC}}$, where $\mu_0 = 4\pi \times 10^{-7}$ H/m is the permeability of free space.

†The gradient field is typically measured in terms of spatial rate of change in the magnetic flux density along the imaging bore axis in teslas per metre (T/m). The magnitude of the magnetic flux density arising from these coils is orders of magnitude smaller than that of the main coils.

acoustic effects in the human head.[30] More recently, a few attempts to analyse the magneto-mechanical coupling in MRI systems have been considered; with the modelling of axisymmetric superconducting solenoids in self magnetic fields[31] and efficient low-order FE solvers for magneto-mechanical coupling in the work of Rausch et al,[32] which utilised calculation of body forces to generate a weakly coupled algorithm. This work was later extended to include acoustic effects in the aforementioned authors' other work.[33]

Our previous work[34] focused on the solution of coupled magneto-mechanical behaviour of geometrically idealised (axisymmetric) MRI scanners, with arbitrarily high-order finite elements,[35,36] through a stress tensor approach to avoid direct calculation of the electromagnetic body forces. Given the relatively small-scale phenomena that emerge in such magnetic and acoustic applications, such as small skin depths in conducting components (known as skin effect)[37] and high frequency acoustic waves, high-order elements are necessary to accurately resolve such effects and ensure accurate solutions, as shown in our other work.[13] Furthermore, by choosing to linearise the transient nonlinear system of coupled equations about the static fields, the formulation simplifies greatly, resulting in a transient linear system of equations dependent on the transient magnetic field excitation, as shown in our other work.[13] Similar techniques, involving the additive split of a nonlinear problem to a series of linear problems, have been successfully applied to the field of computational mechanics, such as analysis of structural membranes,[38-40] high-order mesh generation,[41] and in biomedical applications.[42] This formulation permits a simple *linearised approach* that can be solved in the frequency domain and, given the relatively small frequency ranges of MRI applications, provides rapid solutions to industrial problems. However, the applicability of this linearisation will depend on the strength of the coupling between the acoustic, mechanical, and electromagnetic fields. In the context of MRI scanners, it is thus imperative to answer two important questions: i) how good is the agreement between the computationally efficient *linearised approach* compared with the intensive treatment of the fully nonlinear system, denoted the *nonlinear approach* and (ii) over what range of MRI operating conditions can the *linearised approach* be expected to provide acceptable results for outputs of interest in an industrial context for MRI scanner design? The *nonlinear approach* is trusted as there is no approximation from a physical standpoint.

The aim of this paper is to address these two questions. This is achieved through the following novelties.

1. We revisit the linearisation of the nonlinear equations presented in our other work[13] and provide an alternative formulation, suitable for transient simulation of the full nonlinear problem, using a Newton-Raphson and alpha-type time integration schemes. We refer to this as the *nonlinear approach*.
2. We demonstrate numerically that the *linearised approach* is in excellent agreement with the *nonlinear approach* and derive estimates of the energy present in the *nonlinear approach*, which is not captured by the *linearised approach*.
3. We undertake a rigorous comparison of the *linearised* and *nonlinear approaches* in terms of outputs of interest for a set of challenging industrially motivated examples.

In this paper, we begin by presenting the coupled transient transmission problem and its associated initial conditions in Section 2. Then, in Section 3, we present the continuous weak treatment of the *nonlinear* and *linearised approaches*, derive estimates of the energy not captured by the *linearised approach* and present a transient Newton-Raphson procedure for the nonlinear iteration of the continuous fields in the two approaches. In Section 4, we briefly recall the spatial discretisation of the system by means of high-order finite elements. We include the temporal discretisation, where we have implemented a second order generalised α-scheme, to allow for inclusion of numerical dissipation into the model. The system is then solved through an iterative monolithic Newton-Raphson solution procedure, which is summarised in an algorithm. We then conclude with numerical results in Section 5, which have been obtained by using the in-house software written by the group for this work.

2 | COUPLED SYSTEM

Previously, in our other work,[13] we presented the fully coupled system of nonlinear equations describing the magnetic, mechanic, and acoustic behaviours of an MRI scanner. The work included the transmission conditions present at the interface between the conducting and nonconducting regions, as well as initial and far-field conditions of the system. From this coupled transmission problem, a simpler linearised scheme was introduced by a suitable additive split of the exciting current source $\boldsymbol{J}^s(t)$ as $\boldsymbol{J}^s(t) = \boldsymbol{J}^{\mathrm{DC}} + \boldsymbol{J}^{\mathrm{AC}}(t)$. In this section, we briefly recall the fully coupled transmission problem derived in our earlier paper, describe in detail the physical motivation for the additive split of $\boldsymbol{J}^s(t)$, and provide a set of realistic initial conditions.
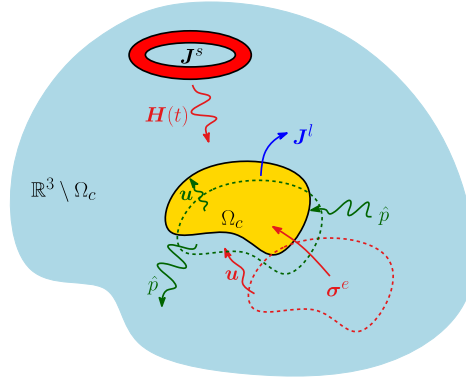
FIGURE 2 Physical representation of the coupling effects in an magnetic resonance imaging (MRI) environment [Colour figure can be viewed at wileyonlinelibrary.com]

2.1 | Transient nonlinear system

The governing coupled transmission problem, illustrated in Figure 2, describing the acousto-magneto-mechanical behaviour of MRI scanners is given by the following. Find $(\boldsymbol{A}, \boldsymbol{u}, \hat{p})(t) \in (\mathbb{R}^3 \times \mathbb{R}^3 \times \mathbb{R})(0, T]$ such that

$$\nabla \times (\mu^{-1} \nabla \times \boldsymbol{A}) + \boldsymbol{J}^e(\boldsymbol{A}) = \boldsymbol{J}^s + \boldsymbol{J}^l(\boldsymbol{A}, \boldsymbol{u}) \qquad \text{in } \mathbb{R}^3, \tag{1a}$$

$$\nabla \cdot \boldsymbol{A} = 0 \qquad \text{in } \mathbb{R}^3 \backslash \Omega_c, \tag{1b}$$

$$\nabla \cdot (\boldsymbol{\sigma}^m(\boldsymbol{u}) + \boldsymbol{\sigma}^e(\boldsymbol{A})) = \rho \boldsymbol{u}_{tt} \qquad \text{in } \Omega_c, \tag{1c}$$

$$\nabla^2 \hat{p} - \frac{1}{c^2} \hat{p}_{tt} = -\nabla \cdot (\nabla \cdot \boldsymbol{\sigma}^e(\boldsymbol{A})) \qquad \text{in } \mathbb{R}^3 \backslash \Omega_c, \tag{1d}$$

$$\boldsymbol{A} = O\left(|\boldsymbol{x}|^{-1}\right), \tag{1e}$$

$$\lim_{|\boldsymbol{x}| \to \infty} \left(\frac{\partial \hat{p}}{\partial |\boldsymbol{x}|} + \hat{p}_t\right) = O\left(|\boldsymbol{x}|^{-1}\right) \qquad \text{as } |\boldsymbol{x}| \to \infty, \tag{1f}$$

$$\boldsymbol{u} = \boldsymbol{u}^D, \tag{1g}$$

$$\nabla \hat{p}|_{\partial \Omega_c^D}^+ \cdot \boldsymbol{n} = 0 \qquad \text{on } \partial \Omega_c^D, \tag{1h}$$

$$\rho^+ \boldsymbol{u}_{tt}|_{\partial \Omega_c^N}^- \cdot \boldsymbol{n} = \left(\nabla \hat{p} + \nabla \cdot \boldsymbol{\sigma}^e(\boldsymbol{A})\right)\Big|_{\partial \Omega_c}^+ \cdot \boldsymbol{n} \qquad \text{on } \partial \Omega_c^N, \tag{1i}$$

$$\boldsymbol{n} \times [\boldsymbol{A}]_{\partial \Omega_c} = \boldsymbol{0}, \tag{1j}$$

$$\boldsymbol{n} \times [\mu^{-1} \nabla \times \boldsymbol{A}]_{\partial \Omega_c} = \boldsymbol{0}, \tag{1k}$$

$$\left(\boldsymbol{\sigma}^e(\boldsymbol{A}) + \boldsymbol{\sigma}^m(\boldsymbol{u})\right)\Big|_{\partial \Omega_c}^- \boldsymbol{n} = \left(\hat{p} \boldsymbol{I} + \boldsymbol{\sigma}^e(\boldsymbol{A})\right)\Big|_{\partial \Omega_c}^+ \boldsymbol{n} \qquad \text{on } \partial \Omega_c, \tag{1l}$$

subject to an appropriate set of initial conditions. In (1), the magnetic flux density $\boldsymbol{B}$ is related to the magnetic field $\boldsymbol{H}$ and the magnetic vector potential $\boldsymbol{A}$ by $\boldsymbol{B} = \mu \boldsymbol{H} = \nabla \times \boldsymbol{A}$, where μ is the magnetic permeability of the medium, $\hat{p}$ is the acoustic pressure field in free-space region (of air) $\mathbb{R}^3 \backslash \Omega_c$, and $\boldsymbol{u}$ is the displacement field of the conducting bodies Ω_c. The eddy currents $\boldsymbol{J}^e(\boldsymbol{A}) = \gamma \boldsymbol{A}_t$ and Lorentz currents $\boldsymbol{J}^l(\boldsymbol{A}, \boldsymbol{u}) = \gamma \boldsymbol{u}_t \times (\nabla \times \boldsymbol{A})$ are expressed in terms of the field variables, respectively. The notation describing the system of equations in (1) is the same as in our other work,[13] where the magnetic vector potential $\boldsymbol{A}$, mechanical displacements $\boldsymbol{u}$, and acoustic pressure $\hat{p}$ have been introduced above. Here, we use $\boldsymbol{u}_t := \partial \boldsymbol{u}/\partial t$ and $\boldsymbol{u}_{tt} := \partial^2 \boldsymbol{u}/\partial t^2$ and note that $\boldsymbol{J}^s$ are the magnetic source currents, $\boldsymbol{x}$ is the position vector, γ is the electrical conductivity, and

$$\boldsymbol{\sigma}^m(\boldsymbol{u}) := \lambda \mathrm{tr}\left(\boldsymbol{\varepsilon}(\boldsymbol{u})\right) \boldsymbol{I} + 2G \boldsymbol{\varepsilon}(\boldsymbol{u}),$$

is the Cauchy stress tensor. In the above, λ and G denote the Lamé parameters, ρ the material density, $\boldsymbol{\varepsilon}(\boldsymbol{u}) := (\nabla \boldsymbol{u} + \nabla \boldsymbol{u}^{\mathrm{T}})/2$ the linear strain tensor, $\boldsymbol{I}$ the identity tensor, $^{\mathrm{T}}$ the transpose, $\boldsymbol{n}$ the unit normal vector, and

$$\boldsymbol{\sigma}^e(\boldsymbol{A}) := \mu^{-1} \left((\nabla \times \boldsymbol{A}) \otimes (\nabla \times \boldsymbol{A}) - \frac{1}{2}|\nabla \times \boldsymbol{A}|^2 \boldsymbol{I}\right), \tag{2}$$

the magnetic component of the Maxwell stress tensor.

The current source $J^s(t)$ in (1) can be decomposed through the additive split $J^s(t) = J^{DC} + J^{AC}(t)$, where J^{DC} is a static current source provided by the main magnet and $J^{AC}(t)$ is a time-varying current source through a series of conducting (gradient) coils. Thus, the supports of J^{DC} and $J^{AC}(t)$ are different and their (maximum) magnitudes and orientations are defined during the MRI design process. In all current MRI designs, they are also chosen so that $|J^{DC}| \gg |J^{AC}|$ by several orders of magnitude to provide a strong background static magnetic field, which is perturbed by weaker time-varying magnetic fields generated from the gradient coils and their interaction with the conducting components. Furthermore, J^{DC} is always present and $J^{AC}(t)$ is only nonzero during imaging sequences.[43] In absence of $J^{AC}(t)$, the system in (1) simplifies considerably as there is no time variation and it is instead described by static solutions $A^{DC}, u^{DC}, \hat{p}^{DC}$.[13] If $\mu = \mu_0 = 4\pi \times 10^{-7}$H/m in $\mathbb{R}^3$, then $u^{DC} = 0$ and $\hat{p}^{DC} = 0$; however, in general, this is not the case.

Taking advantage of the fact that MRI scanners are typically maintained at full field strength, whilst in clinical use, as they are maintained at superconducting temperatures, and that the gradient (time-varying) fields are then only applied during imaging sequences, the initial conditions for (1) are set as the solution of the static field components

$$A(t = 0) = A^{DC} \qquad \text{in } \mathbb{R}^3, \tag{3a}$$

$$u(t = 0) = u^{DC}, u_t(t = 0) = 0 \qquad \text{in } \Omega_c, \tag{3b}$$

$$\hat{p}(t = 0) = \hat{p}^{DC}, \hat{p}_t(t = 0) = 0 \qquad \text{in } \mathbb{R}^3 \backslash \Omega_c. \tag{3c}$$

3 | WEAK TREATMENT OF THE CONTINUOUS PROBLEM

The transient problem described by (1) represents a nonlinear system of coupled equations including electromagnetic, mechanic and acoustic effects in an MRI environment. We first establish the continuous weak form of this coupled *nonlinear approach* and present the continuous weak form of the *linearised approach*, previously derived in our other work.[13] Based on estimates of the energy present in the *nonlinear approach*, which is not captured by the *linearised approach*, presented in the Appendix, we summarise conditions under which we expect the *linearised approach* to provide an accurate representation of the solution of the *nonlinear approach*. A Newton-Raphson iteration is then presented to resolve the nonlinearity in the continuous weak forms.

3.1 | Weak forms of the nonlinear and linearised approaches

3.1.1 | Nonlinear approach

In our *nonlinear approach*, we assume that there exists a fixed point weak continuous solution $(A, u, \hat{p})(t) \in (\tilde{X}(A^{DC}) \times \tilde{Y}(u^{DC}, u^D) \times \tilde{Z}(\hat{p}^{DC}))(0, T]$ of the coupled system (1) satisfying

$$
\begin{aligned}
R_A(A^\delta; A, u, J^s) := &\int_{\mathbb{R}^3} \left((\mu^{-1}\nabla \times A) \cdot (\nabla \times A^\delta) \right) d\Omega + \int_{\Omega_c} \left(\gamma A_t \cdot A^\delta \right) d\Omega \\
&- \int_{\Omega_c} \left((\gamma u_t \times (\nabla \times A)) \cdot A^\delta \right) d\Omega - \int_{\text{supp}(J^s)} (J^s \cdot A^\delta) d\Omega = 0,
\end{aligned} \tag{4a}
$$

$$
\begin{aligned}
R_u(u^\delta; A, u, \hat{p}) := &\int_{\Omega_c} \left((\sigma^m(u) + \sigma^e(A)) : \nabla u^\delta \right) d\Omega + \int_{\Omega_c} \left(\rho u_{tt} \cdot u^\delta \right) d\Omega \\
&- \int_{\partial\Omega_c^N} \left(u^\delta \cdot \left((\hat{p}I + \sigma^e(A)) \big|_{\partial\Omega_c}^+ n \right) \right) dS = 0,
\end{aligned} \tag{4b}
$$

$$
\begin{aligned}
R_{\hat{p}}(\hat{p}^\delta; A, u, \hat{p}) := &\int_{\mathbb{R}^3 \backslash \Omega_c} \left((\nabla \hat{p} + \nabla \cdot \sigma^e(A)) \cdot \nabla \hat{p}^\delta \right) d\Omega + \int_{\mathbb{R}^3 \backslash \Omega_c} \left(\hat{p}^\delta \frac{1}{c^2} \hat{p}_{tt} \right) d\Omega \\
&- \int_{\partial\Omega_c^N} \left(\hat{p}^\delta \left(\rho^+ u_{tt} \big|_{\partial\Omega_c^N}^- \right) \cdot n \right) dS = 0,
\end{aligned} \tag{4c}
$$

for all weighting functions $(\boldsymbol{A}^\delta, \boldsymbol{u}^\delta, \hat{p}^\delta) \in (X \times Y(\boldsymbol{0}) \times Z)$, denoted by a superscript δ, where

$$
\begin{aligned}
\tilde{X}(\boldsymbol{g}) &:= \left\{ \boldsymbol{A} \in X \, : \, \boldsymbol{A}(t=0) = \boldsymbol{g} \operatorname{in} \mathbb{R}^3 \right\}, \\
X &:= \left\{ \boldsymbol{A} \in \boldsymbol{H}(\operatorname{curl}, \mathbb{R}^3) \, : \, \nabla \cdot \boldsymbol{A} = 0 \operatorname{in} \mathbb{R}^3 \backslash \Omega_c \right\}, \\
\tilde{Y}(\boldsymbol{g}, \boldsymbol{h}) &:= \left\{ \boldsymbol{u} \in Y(\boldsymbol{h}) \, : \, \boldsymbol{u}(t=0) = \boldsymbol{g}, \boldsymbol{u}_t(t=0) = \boldsymbol{0} \operatorname{in} \mathbb{R}^3 \right\}, \\
Y(\boldsymbol{h}) &:= \left\{ \boldsymbol{u} \in H^1(\Omega_c)^3 \, : \, \boldsymbol{u} = \boldsymbol{h} \text{ on } \partial\Omega_c^D \right\}, \\
\tilde{Z}(q) &:= \left\{ \hat{p} \in Z \, : \, \hat{p}(t=0) = q, \hat{p}_t(t=0) = 0 \operatorname{in} \mathbb{R}^3 \backslash \Omega_c \right\}, \\
Z &:= \left\{ \hat{p} \in H^1(\mathbb{R}^3 \backslash \Omega_c) \right\},
\end{aligned}
$$

and $\boldsymbol{H}(\operatorname{curl}, \mathbb{R}^3)$ and $H^1(\mathbb{R}^3)$ have their usual definitions, eg, the work of Monk.[44]

3.1.2 | Linearised approach

The continuous version of the *linearised approach*, previously derived in our other work,[13] corresponds to seeking weak solutions $(\boldsymbol{A}^{\mathrm{DC}} + \boldsymbol{A}^{\mathrm{AC}}(t)), (\boldsymbol{u}^{\mathrm{DC}} + \boldsymbol{u}^{\mathrm{AC}}(t)), (\hat{p}^{\mathrm{DC}} + \hat{p}^{\mathrm{AC}}(t))$, which are obtained from a direct current DC and an alternating current AC stage.

DC-stage

The static solutions $(\boldsymbol{A}^{\mathrm{DC}}, \boldsymbol{u}^{\mathrm{DC}}, \hat{p}^{\mathrm{DC}}) \in (X \times Y(\boldsymbol{u}^{\mathrm{D}}) \times Z)$ are the fixed point solution of

$$
\begin{aligned}
R_A^{\mathrm{DC}}(\boldsymbol{A}^\delta; \boldsymbol{A}^{\mathrm{DC}}, \boldsymbol{u}^{\mathrm{DC}}) &:= R_A(\boldsymbol{A}^\delta; \boldsymbol{A}^{\mathrm{DC}}, \boldsymbol{u}^{\mathrm{DC}}, \boldsymbol{J}^{\mathrm{DC}}) \\
&= \int_{\mathbb{R}^3} \left((\mu^{-1} \nabla \times \boldsymbol{A}^{\mathrm{DC}}) \cdot (\nabla \times \boldsymbol{A}^\delta) \right) \mathrm{d}\Omega - \int_{\operatorname{supp}(\boldsymbol{J}^{\mathrm{DC}})} (\boldsymbol{J}^{\mathrm{DC}} \cdot \boldsymbol{A}^\delta) \mathrm{d}\Omega = 0,
\end{aligned}
\tag{5a}
$$

$$
\begin{aligned}
R_u^{\mathrm{DC}}(\boldsymbol{u}^\delta; \boldsymbol{A}^{\mathrm{DC}}, \boldsymbol{u}^{\mathrm{DC}}, \hat{p}^{\mathrm{DC}}) &:= R_u(\boldsymbol{u}^\delta; \boldsymbol{A}^{\mathrm{DC}}, \boldsymbol{u}^{\mathrm{DC}}, \hat{p}^{\mathrm{DC}}) \\
&= \int_{\Omega_c} \left((\boldsymbol{\sigma}^m(\boldsymbol{u}^{\mathrm{DC}}) + \boldsymbol{\sigma}^e(\boldsymbol{A}^{\mathrm{DC}})) : \nabla \boldsymbol{u}^\delta \right) \mathrm{d}\Omega \\
&\quad - \int_{\partial\Omega_c^N} \left(\boldsymbol{u}^\delta \cdot \left((\hat{p}^{\mathrm{DC}} \boldsymbol{I} + \boldsymbol{\sigma}^e(\boldsymbol{A}^{\mathrm{DC}})) \Big|_{\partial\Omega_c}^+ \boldsymbol{n} \right) \right) \mathrm{d}S = 0,
\end{aligned}
\tag{5b}
$$

$$
\begin{aligned}
R_{\hat{p}}^{\mathrm{DC}}(\hat{p}^\delta; \boldsymbol{A}^{\mathrm{DC}}, \boldsymbol{u}^{\mathrm{DC}}, \hat{p}^{\mathrm{DC}}) &:= R_{\hat{p}}(\hat{p}^\delta; \boldsymbol{A}^{\mathrm{DC}}, \boldsymbol{u}^{\mathrm{DC}}, \hat{p}^{\mathrm{DC}}) \\
&= \int_{\mathbb{R}^3 \backslash \Omega_c} \left((\nabla \hat{p}^{\mathrm{DC}} + \nabla \cdot \boldsymbol{\sigma}^e(\boldsymbol{A}^{\mathrm{DC}})) \cdot \nabla \hat{p}^\delta \right) \mathrm{d}\Omega = 0,
\end{aligned}
\tag{5c}
$$

for all $(\boldsymbol{A}^\delta, \boldsymbol{u}^\delta, \hat{p}^\delta) \in (X \times Y(\boldsymbol{0}) \times Z)$.

AC-stage

The transient weak solutions $(\boldsymbol{A}^{\mathrm{AC}}, \boldsymbol{u}^{\mathrm{AC}}, \hat{p}^{\mathrm{AC}})(t) \in (\tilde{X}(\boldsymbol{0}) \times \tilde{Y}(\boldsymbol{0}, \boldsymbol{0}) \times \tilde{Z}(0))(0, T]$ are the solution of the linearised problem

$$
DR_A(\boldsymbol{A}^\delta; \boldsymbol{A}^{\mathrm{DC}}, \boldsymbol{u}^{\mathrm{DC}})[\boldsymbol{A}^{\mathrm{AC}}] + DR_A(\boldsymbol{A}^\delta; \boldsymbol{A}^{\mathrm{DC}}, \boldsymbol{u}^{\mathrm{DC}})[\boldsymbol{u}^{\mathrm{AC}}] = -R_A(\boldsymbol{A}^\delta; \boldsymbol{A}^{\mathrm{DC}}, \boldsymbol{u}^{\mathrm{DC}}, \boldsymbol{J}^s),
\tag{6a}
$$

$$
\begin{aligned}
DR_u(\boldsymbol{u}^\delta; \boldsymbol{A}^{\mathrm{DC}}, \boldsymbol{u}^{\mathrm{DC}}, \hat{p}^{\mathrm{DC}})[\boldsymbol{A}^{\mathrm{AC}}] &+ DR_u(\boldsymbol{u}^\delta; \boldsymbol{A}^{\mathrm{DC}}, \boldsymbol{u}^{\mathrm{DC}}, \hat{p}^{\mathrm{DC}})[\boldsymbol{u}^{\mathrm{AC}}] + \\
DR_u(\boldsymbol{u}^\delta; \boldsymbol{A}^{\mathrm{DC}}, \boldsymbol{u}^{\mathrm{DC}}, \hat{p}^{\mathrm{DC}})[\hat{p}^{\mathrm{AC}}] &= -R_u(\boldsymbol{u}^\delta; \boldsymbol{A}^{\mathrm{DC}}, \boldsymbol{u}^{\mathrm{DC}}, \hat{p}^{\mathrm{DC}}),
\end{aligned}
\tag{6b}
$$

$$
\begin{aligned}
DR_{\hat{p}}(\hat{p}^\delta; \boldsymbol{A}^{\mathrm{DC}}, \boldsymbol{u}^{\mathrm{DC}}, \hat{p}^{\mathrm{DC}})[\boldsymbol{A}^{\mathrm{AC}}] &+ DR_{\hat{p}}(\hat{p}^\delta; \boldsymbol{A}^{\mathrm{DC}}, \boldsymbol{u}^{\mathrm{DC}}, \hat{p}^{\mathrm{DC}})[\boldsymbol{u}^{\mathrm{AC}}] + \\
DR_{\hat{p}}(\hat{p}^\delta; \boldsymbol{A}^{\mathrm{DC}}, \boldsymbol{u}^{\mathrm{DC}}, \hat{p}^{\mathrm{DC}})[\hat{p}^{\mathrm{AC}}] &= -R_{\hat{p}}(\hat{p}^\delta; \boldsymbol{A}^{\mathrm{DC}}, \boldsymbol{u}^{\mathrm{DC}}, \hat{p}^{\mathrm{DC}}),
\end{aligned}
\tag{6c}
$$

for all $(\boldsymbol{A}^\delta, \boldsymbol{u}^\delta, \hat{p}^\delta) \in (X \times Y(\boldsymbol{0}) \times Z)$ under the assumption $(\boldsymbol{A}^{\mathrm{AC}}, \boldsymbol{u}^{\mathrm{AC}}, \hat{p}^{\mathrm{AC}})(t)$ are small perturbations from $(\boldsymbol{A}^{\mathrm{DC}}, \boldsymbol{u}^{\mathrm{DC}}, \hat{p}^{\mathrm{DC}})$. In the above, the notation $DR_A(\boldsymbol{A}^\delta; \boldsymbol{A}^{\mathrm{DC}}, \boldsymbol{u}^{\mathrm{DC}})[\boldsymbol{A}^{\mathrm{AC}}]$ denotes the directional derivative of R_A about the static solutions

$(\boldsymbol{A}^{\mathrm{DC}}, \boldsymbol{u}^{\mathrm{DC}})$ in the direction $\boldsymbol{A}^{\mathrm{AC}}$ with similar meanings for the other terms.[45] By deriving the required terms, this can be explicitly written as: Find $(\boldsymbol{A}^{\mathrm{AC}}, \boldsymbol{u}^{\mathrm{AC}}, \hat{p}^{\mathrm{AC}})(t) \in (\tilde{X}(\boldsymbol{0}) \times \tilde{Y}(\boldsymbol{0}, \boldsymbol{0}) \times \tilde{Z}(0))(0, T]$ such that

$$
\int_{\mathbb{R}^3} \left((\mu^{-1}\nabla \times \boldsymbol{A}^{\mathrm{AC}}) \cdot (\nabla \times \boldsymbol{A}^{\delta}) \right) \mathrm{d}\Omega + \int_{\Omega_c} \left(\gamma (\boldsymbol{A}^{\mathrm{AC}})_t \cdot \boldsymbol{A}^{\delta} \right) \mathrm{d}\Omega
$$
$$
- \int_{\Omega_c} \left(\left(\gamma (\boldsymbol{u}^{\mathrm{AC}})_t \times (\nabla \times \boldsymbol{A}^{\mathrm{DC}}) \right) \cdot \boldsymbol{A}^{\delta} \right) \mathrm{d}\Omega - \int_{\mathrm{supp}(\boldsymbol{J}^{\mathrm{AC}})} (\boldsymbol{J}^{\mathrm{AC}} \cdot \boldsymbol{A}^{\delta}) \mathrm{d}\Omega = 0, \tag{7a}
$$

$$
\int_{\Omega_c} \left(\left(\boldsymbol{\sigma}^m(\boldsymbol{u}^{\mathrm{AC}}) + \mu^{-1} S(\boldsymbol{A}^{\mathrm{DC}}, \boldsymbol{A}^{\mathrm{AC}}) \right) : \nabla \boldsymbol{u}^{\delta} \right) \mathrm{d}\Omega + \int_{\Omega_c} \left(\rho (\boldsymbol{u}^{\mathrm{AC}})_{tt} \cdot \boldsymbol{u}^{\delta} \right) \mathrm{d}\Omega
$$
$$
- \int_{\partial\Omega_c^N} \left(\boldsymbol{u}^{\delta} \cdot \left(\left. \left(\hat{p}^{\mathrm{AC}} \boldsymbol{I} + \mu^{-1} S(\boldsymbol{A}^{\mathrm{DC}}, \boldsymbol{A}^{\mathrm{AC}}) \right) \right|_{\partial\Omega_c}^{+} \boldsymbol{n} \right) \right) \mathrm{d}S = 0, \tag{7b}
$$

$$
\int_{\mathbb{R}^3 \setminus \Omega_c} \left(\left(\nabla \hat{p}^{\mathrm{AC}} + \nabla \cdot \boldsymbol{\sigma}^e(\boldsymbol{A}^{\mathrm{AC}}) \right) \cdot \nabla \hat{p}^{\delta} \right) \mathrm{d}\Omega + \int_{\mathbb{R}^3 \setminus \Omega_c} \left(\frac{1}{c^2} (\hat{p}^{\mathrm{AC}})_{tt} \hat{p}^{\delta} \right) \mathrm{d}\Omega
$$
$$
- \int_{\partial\Omega_c^N} \left(\hat{p}^{\delta} \left(\rho^+ \left. (\boldsymbol{u}^{\mathrm{AC}})_{tt} \right|_{\partial\Omega_c^N}^{-} \right) \cdot \boldsymbol{n} \right) \mathrm{d}S = 0, \tag{7c}
$$

for all $(\boldsymbol{A}^{\delta}, \boldsymbol{u}^{\delta}, \hat{p}^{\delta}) \in (X \times Y(\boldsymbol{0}) \times Z)$. In the above, the linearised electromagnetic stress tensor, introduced previously in our other work,[13] is

$$
S(\boldsymbol{a}, \boldsymbol{b}) := (\nabla \times \boldsymbol{a}) \otimes (\nabla \times \boldsymbol{b}) + (\nabla \times \boldsymbol{a}) \otimes (\nabla \times \boldsymbol{b}) - ((\nabla \times \boldsymbol{a}) \cdot (\nabla \times \boldsymbol{b})) \boldsymbol{I}.
$$

3.2 | Energy not captured by the linearised approach

In the Appendix, we estimate the energy present in the *nonlinear approach*, which is not captured by the *linearised approach*. We find that this will be small, at a continuous level, provided the following criteria are met for all time t:

1. $||\gamma (\boldsymbol{u}^{\mathrm{AC}})_t(t)||_{L^{\infty}(\Omega_c)} ||\boldsymbol{B}^{\mathrm{DC}}||^2_{L^{\infty}(\Omega_c)} \ll 1$,
2. $||\boldsymbol{B}^{\mathrm{AC}}(t)||^2_{L^{\infty}(\Omega_c)} (||\nabla \boldsymbol{u}^{\mathrm{DC}}||_{L^{\infty}(\Omega_c)} + ||\nabla \boldsymbol{u}^{\mathrm{AC}}||_{L^{\infty}(\Omega_c)}) \ll 1$, $||\boldsymbol{B}^{\mathrm{AC}}(t)||^2_{L^{\infty}(\partial\Omega_c^N)} (||\boldsymbol{u}^{\mathrm{DC}}||_{L^{\infty}(\partial\Omega_c^N)} + ||\boldsymbol{u}^{\mathrm{AC}}||_{L^{\infty}(\partial\Omega_c^N)}) \ll 1$,
3. $\mu_0 ||\boldsymbol{H}^{\mathrm{AC}}(t)||_{L^{\infty}(\mathrm{supp}(\boldsymbol{J}^{\mathrm{AC}}))} ||\boldsymbol{J}^{\mathrm{AC}}||_{L^{\infty}(\mathrm{supp}(\boldsymbol{J}^{\mathrm{AC}}))} ||\nabla \hat{p}^{\mathrm{DC}}||_{L^{\infty}(\mathrm{supp}(\boldsymbol{J}^{\mathrm{AC}}))} + ||\nabla \hat{p}^{\mathrm{AC}}||_{L^{\infty}(\mathrm{supp}(\boldsymbol{J}^{\mathrm{AC}}))} \ll 1$,
4. $||\boldsymbol{B}^{\mathrm{AC}}(t)||_{L^{\infty}(\Omega_c)} / ||\boldsymbol{B}^{\mathrm{DC}}||_{L^{\infty}(\Omega_c)} \ll 1$.

Provided that these conditions hold, we conjecture that the *linearised approach* will be in good agreement with the *nonlinear approach*. We argue that these conditions will be met on physical grounds for MRI scanners as follows: 1) requires that the velocities are small in comparison to γ and $||\boldsymbol{B}^{\mathrm{DC}}||^2_{L^{\infty}(\Omega_c)}$, which is typically the case for MRI scanners; 2) requires that the displacements and strains (displacement gradients) are small in comparison to $||\boldsymbol{B}^{\mathrm{AC}}||^2_{L^{\infty}(\Omega_c)}$ and $||\boldsymbol{B}^{\mathrm{AC}}||^2_{L^{\infty}(\partial\Omega_c^N)}$, which is again typically the case for MRI scanners; 3) requires the pressure gradients in the coils are small, which is typically the case for MRI scanners under the Biot-Savart coil assumption; and 4) requires the $\boldsymbol{B}^{\mathrm{DC}}$ field obtained from the strong main magnet results in a $||\boldsymbol{B}^{\mathrm{DC}}||_{L^{\infty}(\Omega_c)}$ that is orders of magnitude larger than $||\boldsymbol{B}^{\mathrm{AC}}||_{L^{\infty}(\Omega_c)}$, obtained from the weaker AC coils and smaller field perturbations caused by eddy and Lorentz currents in the conductors. In Section 5, we will demonstrate numerically that the 2 approaches are in excellent agreement for such problems. We include a simple model below to illustrate the applicability of these criteria.

3.2.1 | Simple model relating field and current strengths

Whilst the true field strength $\boldsymbol{B} = \mu \boldsymbol{H}$ can only be found after solving (1) by means of the solution of the continuous weak forms for the *nonlinear* or *linearised approaches*, described in Sections 3.1.1 and 3.1.2, there is merit in also considering a simple model to relate $\boldsymbol{B}$ to the applied current density in the coils. This is because manufacturer's data, available for MRI scanners, is typically only quoted in terms of the maximum capable main and gradient field strengths at the central axis of the imaging bore.[6-8] Therefore, to determine the operating ranges of the current densities on in-use scanners, the relationships given by this simplified model offer useful insight.

In the simplified model, as shown in Figure 3, all transient, eddy current, and coupling effects are neglected, as is the mutual inductance between coils. Coil i has a constant cross-sectional area a_i, is circular, and hence, rotationally symmetric and so is best expressed in terms of cylindrical coordinates (r, ϕ, z) and carries a uniform current density
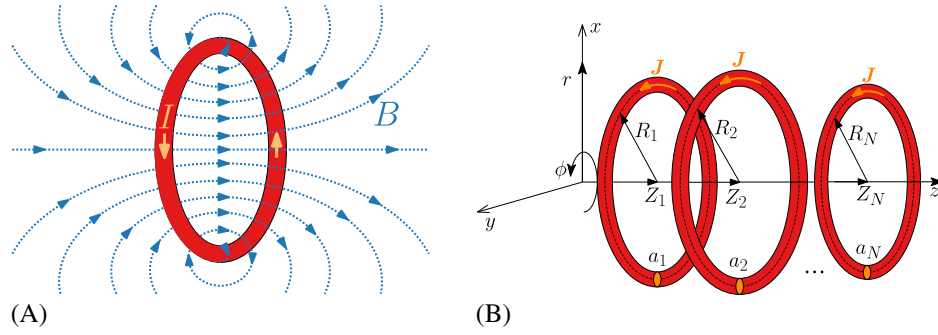
FIGURE 3 Single current loop, representing a lumped mass of coils. A, Magnetic field around single current loop; B, Multiple coil configuration [Colour figure can be viewed at wileyonlinelibrary.com]

$J^s = J^s_\phi e_\phi$. Then, by an additive application of the Biot-Savart law for a single coil,[46] the following relationship can be derived for the field strength along the axis $r = 0$ for N coils placed at different locations (R_i, Z_i)

$$|J^s| = \sum_i^N \frac{\left((z - Z_i)^2 + R_i^2\right)^{3/2}}{R_i a_i} |B(0, \phi, z)|, \tag{8}$$

where $B(0, \phi, z) = B_z(r = 0, z)e_z$ along this axis, R_i is the radius, and Z_i the axial position of the *ith* current source relative to the scanner's central axes. Provided the aforementioned assumptions are enforced, this relationship can be applied to obtain the current densities that are associated only with the main magnet ($J^s = J^{DC}$) or with the gradient coil ($J^s = J^{AC}$) from their produced field strengths. It also provides a guide as to the ranges of ratios of $|J^{AC}|/|J^{DC}|$ and $||B^{AC}||_{L^\infty(\Omega)}/||B^{DC}||_{L^\infty(\Omega)}$ over which the *linearised approach* is applicable.

3.3 | Nonlinear iteration

We now present a nonlinear iteration to resolve the nonlinear terms present in (4) and (5), resulting in linearised problems (not to be confused with *linearised approach*) being solved at each iteration. The unknowns in the linearised problems are continuous update fields, which we relate to the continuous solution of (4) and (5). We make explicit those terms, which are time dependent.

3.3.1 | Newton-Raphson for the nonlinear approach

To resolve the nonlinearity in (4) a nonlinear iteration, which requires the solution of a linearised problem at each iteration, is performed. This is expressed in the form of the following iterative Newton-Raphson procedure: Find $(\delta_A^{[k]}, \delta_u^{[k]}, \delta_{\hat{p}}^{[k]})(t) \in \tilde{X}(\mathbf{0}) \times \tilde{Y}(\mathbf{0}, \mathbf{0}) \times \tilde{Z}(\mathbf{0})(0, T]$ such that

$$DR_A\left(A^\delta; A^{[k]}, u^{[k]}\right)\left[\delta_A^{[k]}\right] + DR_A\left(A^\delta; A^{[k]}, u^{[k]}\right)\left[\delta_u^{[k]}\right]$$
$$= -R_A\left(A^\delta; A^{[k]}, u^{[k]}\right), \tag{9a}$$

$$DR_u\left(u^\delta; A^{[k]}, u^{[k]}, \hat{p}^{[k]}\right)\left[\delta_A^{[k]}\right] + DR_u\left(u^\delta; A^{[k]}, u^{[k]}, \hat{p}^{[k]}\right)\left[\delta_u^{[k]}\right] + DR_u\left(u^\delta; A^{[k]}, u^{[k]}, \hat{p}^{[k]}\right)\left[\delta_{\hat{p}}^{[k]}\right]$$
$$= -R_u\left(u^\delta; A^{[k]}, u^{[k]}, \hat{p}^{[k]}\right), \tag{9b}$$

$$DR_{\hat{p}}\left(\hat{p}^\delta; A^{[k]}, u^{[k]}, \hat{p}^{[k]}\right)\left[\delta_A^{[k]}\right] + DR_{\hat{p}}\left(\hat{p}^\delta; A^{[k]}, u^{[k]}, \hat{p}^{[k]}\right)\left[\delta_u^{[k]}\right] + DR_{\hat{p}}\left(\hat{p}^\delta; A^{[k]}, u^{[k]}, \hat{p}^{[k]}\right)\left[\delta_{\hat{p}}^{[k]}\right]$$
$$= -R_{\hat{p}}\left(\hat{p}^\delta; A^{[k]}, u^{[k]}, \hat{p}^{[k]}\right), \tag{9c}$$

for all $(A^\delta, u^\delta, \hat{p}^\delta) \in X \times Y(\mathbf{0}) \times Z$ for a particular iteration $[k]$, where

$$A^{[k+1]}(t) = A^{[k]}(t) + \delta_A^{[k]}(t), \tag{10a}$$

$$u^{[k+1]}(t) = u^{[k]}(t) + \delta_u^{[k]}(t), \tag{10b}$$

$$\hat{p}^{[k+1]}(t) = \hat{p}^{[k]}(t) + \delta_{\hat{p}}^{[k]}(t). \tag{10c}$$

As standard, this linearisation is established under the assumption that the updates $(\delta_A^{[k]}, \delta_u^{[k]}, \delta_{\hat{p}}^{[k]})(t)$ are small.[45] Given an initial guess $(\boldsymbol{A}^{[0]}, \boldsymbol{u}^{[0]}, \hat{p}^{[0]})(t) \in \tilde{X}(\boldsymbol{A}^{\mathrm{DC}}) \times \tilde{Y}(\boldsymbol{u}^{\mathrm{DC}}, \boldsymbol{u}^D) \times \tilde{Z}(\hat{p}^{\mathrm{DC}})$, and performing iterations of this kind, leads to a sequence of continuous iterates

$$\left(\boldsymbol{A}^{[0]}, \boldsymbol{u}^{[0]}, \hat{p}^{[0]}\right)(t), \left(\boldsymbol{A}^{[1]}, \boldsymbol{u}^{[1]}, \hat{p}^{[1]}\right)(t), (\boldsymbol{A}^{[2]}, \boldsymbol{u}^{[2]}, \hat{p}^{[2]})(t), \cdots \in \tilde{X}(\boldsymbol{A}^{\mathrm{DC}}) \times \tilde{Y}(\boldsymbol{u}^{\mathrm{DC}}, \boldsymbol{u}^D) \times \tilde{Z}(\hat{p}^{\mathrm{DC}})(0, T]$$

with the goal of converging to the continuous solution $(\boldsymbol{A}, \boldsymbol{u}, \hat{p})(t) \in (\tilde{X}(\boldsymbol{A}^{\mathrm{DC}}) \times \tilde{Y}(\boldsymbol{u}^{\mathrm{DC}}, \boldsymbol{u}^D) \times \tilde{Z}(\hat{p}^{\mathrm{DC}}))(0, T]$ of (4). Provided the initial guess $(\boldsymbol{A}^{[0]}, \boldsymbol{u}^{[0]}, \hat{p}^{[0]})(t)$ is chosen to be sufficiently close to $(\boldsymbol{A}, \boldsymbol{u}, \hat{p})(t)$ this is expected to be the case. The requirements for the convergence of Newton-Raphson schemes are well documented and are consequently not discussed further, see e.g.[45]

It is instructive to introduce the notation $\boldsymbol{q}(t) := (\boldsymbol{q}_A, \boldsymbol{q}_u, q_{\hat{p}})(t) = (\boldsymbol{A}, \boldsymbol{u}, \hat{p})(t)$ and to rewrite (9) in the form of the Newton-Raphson iteration: Find $\delta_q^{[k]}(t) \in \tilde{W}(\boldsymbol{0}, \boldsymbol{0})(0, T]$ such that

$$M\left(\left(\delta_q^{[k]}\right)_{tt}, \boldsymbol{q}^\delta\right) + C\left(\left(\delta_q^{[k]}\right)_t, \boldsymbol{q}^\delta; \boldsymbol{q}^{[k]}\right) + K\left(\delta_q^{[k]}, \boldsymbol{q}^\delta; \boldsymbol{q}^{[k]}, \left(\boldsymbol{q}^{[k]}\right)_t\right) = \\ - R_q\left(\boldsymbol{q}^\delta; \boldsymbol{q}^{[k]}, \left(\boldsymbol{q}^{[k]}\right)_t, \left(\boldsymbol{q}^{[k]}\right)_{tt}, \boldsymbol{J}^s\right), \tag{11}$$

for all $\boldsymbol{q}^\delta \in W(\boldsymbol{0})$, where

$$\boldsymbol{q}^{[k+1]}(t) = \boldsymbol{q}^{[k]}(t) + \delta_q^{[k]}(t), \tag{12}$$

and $\tilde{W}(\boldsymbol{q}^{\mathrm{DC}}, \boldsymbol{u}^D) = \tilde{X}(\boldsymbol{A}^{\mathrm{DC}}) \times \tilde{Y}(\boldsymbol{u}^{\mathrm{DC}}, \boldsymbol{u}^D) \times \tilde{Z}(\hat{p}^{\mathrm{DC}})$ and $W(\boldsymbol{u}^D) := X \times Y(\boldsymbol{u}^D) \times Z$. As before, if $\boldsymbol{q}^{[0]} \in \tilde{W}(\boldsymbol{q}^{\mathrm{DC}}, \boldsymbol{u}_D)$ is chosen sufficiently close to $\boldsymbol{q} \in \tilde{W}(\boldsymbol{q}^{\mathrm{DC}}, \boldsymbol{u}^D)$ then the iterates $\boldsymbol{q}^{[0]}(t), \boldsymbol{q}^{[1]}(t), \boldsymbol{q}^{[2]}(t), \ldots \in \tilde{W}(\boldsymbol{q}^{\mathrm{DC}}, \boldsymbol{u}^D)$ are expected to converge to $\boldsymbol{q}(t) \in \tilde{W}(\boldsymbol{q}^{\mathrm{DC}}, \boldsymbol{u}^D)$. This formulation has the benefit that the forms of M, C, and K, are associated with the mass, damping, and stiffness contributions to the system, respectively, and can be found to be[‡]

$$M\left(\left(\delta_q^{[k]}\right)_{tt}, \boldsymbol{q}^\delta\right) := \int_{\Omega_c} \left(\rho\left(\delta_u^{[k]}\right)_{tt} \cdot \boldsymbol{q}_u^\delta\right) \mathrm{d}\Omega - \int_{\partial\Omega_c^N} \left(q_{\hat{p}}^\delta\left(\rho^+\left(\delta_u^{[k]}\right)_{tt}\Big|^-\right) \cdot \boldsymbol{n}^+\right) \mathrm{d}S \\ + \int_{\mathbb{R}^3 \backslash \Omega_c} \left(\frac{1}{c^2}\left(\delta_{\hat{p}}^{[k]}\right)_{tt} q_{\hat{p}}^\delta\right) \mathrm{d}\Omega, \tag{13a}$$

$$C\left(\left(\delta_q^{[k]}\right)_t, \boldsymbol{q}^\delta; \boldsymbol{q}^{[k]}\right) := \int_{\mathbb{R}^3} \left(\gamma\left(\delta_A^{[k]}\right)_t \cdot \boldsymbol{q}_A^\delta\right) \mathrm{d}\Omega - \int_{\Omega_c} \left(\left(\gamma\left(\delta_u^{[k]}\right)_t \times \left(\nabla \times \boldsymbol{q}_A^{[k]}\right)\right) \cdot \boldsymbol{q}_A^\delta\right) \mathrm{d}\Omega, \tag{13b}$$

$$K\left(\delta_q^{[k]}, \boldsymbol{q}^\delta; \boldsymbol{q}^{[k]}, \left(\boldsymbol{q}^{[k]}\right)_t\right) := \int_{\mathbb{R}^3} \left(\mu^{-1}\left(\nabla \times \delta_A^{[k]}\right) \cdot \left(\nabla \times \boldsymbol{q}_A^\delta\right)\right) \mathrm{d}\Omega - \int_{\Omega_c} \left(\left(\gamma\left(\boldsymbol{q}_u^{[k]}\right)_t \times \left(\nabla \times \delta_A^{[k]}\right)\right) \cdot \boldsymbol{q}_A^\delta\right) \mathrm{d}\Omega$$

$$+ \int_{\Omega_c} \left(\mu^{-1} S\left(\boldsymbol{q}_A^{[k]}, \delta_A^{[k]}\right) : \nabla\boldsymbol{q}_u^\delta\right) \mathrm{d}\Omega - \int_{\partial\Omega_c^N} \left(\boldsymbol{q}_u^\delta \cdot \left(\mu_0^{-1} S\left(\boldsymbol{q}_A^{[k]}, \delta_A^{[k]}\right)\big|^+ \boldsymbol{n}^-\right)\right) \mathrm{d}S$$

$$+ \int_{\Omega_c} \left(\boldsymbol{\sigma}^m\left(\delta_u^{[k]}\right) : \nabla\boldsymbol{q}_u^\delta\right) \mathrm{d}\Omega - \int_{\partial\Omega_c^N} \left(\delta_{\hat{p}}^{[k]}\big|^+ \boldsymbol{n}^- \cdot \boldsymbol{q}_u^\delta\right) \mathrm{d}S$$

$$- \int_{\mathrm{supp}(\boldsymbol{J}^s)} \left(\left(\nabla \times \delta_A^{[k]} \times \left(\nabla \times \left(\mu_0^{-1}\nabla \times \boldsymbol{q}_A^{[k]}\right)\right)\right.\right.$$

$$+ \left.\left. \nabla \times \boldsymbol{q}_A^{[k]} \times \left(\nabla \times \left(\mu_0^{-1}\nabla \times \delta_A^{[k]}\right)\right)\right) \cdot \nabla q_{\hat{p}}^\delta\right) \mathrm{d}\Omega$$

$$+ \int_{\mathbb{R}^3 \backslash \Omega_c} \left(\nabla\delta_{\hat{p}}^{[k]} \cdot \nabla q_{\hat{p}}^\delta\right) \mathrm{d}\Omega. \tag{13c}$$

The system residual R_q easily follows from (4) and is defined as

$$R_q\left(\boldsymbol{q}^\delta; \boldsymbol{q}^{[k]}, \left(\boldsymbol{q}^{[k]}\right)_t, P\left(\boldsymbol{q}^{[k]}\right)_{tt}, \boldsymbol{J}^s\right) := M\left(\left(\boldsymbol{q}^{[k]}\right)_{tt}, \boldsymbol{q}^\delta\right) + C\left(\left(\boldsymbol{q}^{[k]}\right)_t, \boldsymbol{q}^\delta; \boldsymbol{q}^{[k]}\right)$$

$$+ \int_{\mathbb{R}^3} \left(\mu^{-1}\left(\nabla \times \boldsymbol{q}_A^{[k]}\right) \cdot \left(\nabla \times \boldsymbol{q}_A^\delta\right)\right) \mathrm{d}\Omega + \int_{\Omega_c} \left(\left(\boldsymbol{\sigma}^m\left(\boldsymbol{q}_u^{[k]}\right) + \boldsymbol{\sigma}^e\left(\boldsymbol{q}_A^{[k]}\right)\right) : \nabla\boldsymbol{q}_u^\delta\right) \mathrm{d}\Omega$$

$$- \int_{\partial\Omega_C^N} \left(\boldsymbol{q}_u^\delta \cdot \left(\left(q_{\hat{p}}^{[k]}\boldsymbol{I} + \boldsymbol{\sigma}^e\left(\boldsymbol{q}_A^{[k]}\right)\right)\big|^+ \boldsymbol{n}^-\right)\right) \mathrm{d}S + \int_{\mathbb{R}^3 \backslash \Omega_c} \left(\nabla q_{\hat{p}}^{[k]} \cdot \nabla q_{\hat{p}}^\delta + \left(\nabla \cdot \boldsymbol{\sigma}^e\left(\boldsymbol{q}_A^{[k]}\right)\right) \cdot \nabla q_{\hat{p}}^\delta\right) \mathrm{d}\Omega$$

$$- \int_{\mathbb{R}^3} \left(\boldsymbol{J}^s(t) \cdot \boldsymbol{q}_A^\delta\right) \mathrm{d}\Omega. \tag{14}$$

[‡]The directional derivatives in (9a) are already stated in our other work[13] and consequently not repeated here.

3.3.2 | Newton-Raphson for the linearised approach

DC-Stage

A nonlinear iteration, with a linearised problem being solved at each iteration, is also required to resolve the nonlinearity in (7). For this, we employ the Newton-Raphson procedure: Find $(\delta_A^{\mathrm{DC}[k]}, \delta_u^{\mathrm{DC}[k]}, \delta_{\hat{p}}^{\mathrm{DC}[k]}) \in X \times Y(\mathbf{0}) \times Z$ such that

$$DR_A^{\mathrm{DC}}\left(\mathbf{A}^\delta; \mathbf{A}^{\mathrm{DC}[k]}\right)\left[\delta_A^{\mathrm{DC}[k]}\right] = -R_A^{\mathrm{DC}}\left(\mathbf{A}^\delta; \mathbf{A}^{\mathrm{DC}[k]}\right), \tag{15a}$$

$$DR_u^{\mathrm{DC}}\left(\mathbf{u}^\delta; \mathbf{A}^{\mathrm{DC}[k]}, \mathbf{u}^{\mathrm{DC}[k]}, \hat{p}^{\mathrm{DC}[k]}\right)\left[\delta_A^{\mathrm{DC}[k]}\right] + DR_u^{\mathrm{DC}}\left(\mathbf{u}^\delta; \mathbf{A}^{\mathrm{DC}[k]}, \mathbf{u}^{\mathrm{DC}[k]}, \hat{p}^{\mathrm{DC}[k]}\right)\left[\delta_u^{\mathrm{DC}[k]}\right]$$

$$+ DR_u^{\mathrm{DC}}\left(\mathbf{u}^\delta; \mathbf{A}^{\mathrm{DC}[k]}, \mathbf{u}^{\mathrm{DC}[k]}, \hat{p}^{\mathrm{DC}[k]}\right)\left[\delta_{\hat{p}}^{\mathrm{DC}[k]}\right] = -R_u^{\mathrm{DC}}\left(\mathbf{u}^\delta; \mathbf{A}^{\mathrm{DC}[k]}, \mathbf{u}^{\mathrm{DC}[k]}, \hat{p}^{\mathrm{DC}[k]}\right), \tag{15b}$$

$$DR_{\hat{p}}^{\mathrm{DC}}\left(\hat{p}^\delta; \mathbf{A}^{\mathrm{DC}[k]}, \mathbf{u}^{\mathrm{DC}[k]}, \hat{p}^{\mathrm{DC}[k]}\right)\left[\delta_A^{\mathrm{DC}[k]}\right] + DR_{\hat{p}}^{\mathrm{DC}}\left(\hat{p}^\delta; \mathbf{A}^{\mathrm{DC}[k]}, \mathbf{u}^{\mathrm{DC}[k]}, \hat{p}^{\mathrm{DC}[k]}\right)\left[\delta_u^{\mathrm{DC}[k]}\right]$$

$$+ DR_{\hat{p}}^{\mathrm{DC}}\left(\hat{p}^\delta; \mathbf{A}^{\mathrm{DC}[k]}, \mathbf{u}^{\mathrm{DC}[k]}, \hat{p}^{\mathrm{DC}[k]}\right)\left[\delta_{\hat{p}}^{\mathrm{DC}[k]}\right] = -R_{\hat{p}}^{\mathrm{DC}}\left(\hat{p}^\delta; \mathbf{A}^{\mathrm{DC}[k]}, \mathbf{u}^{\mathrm{DC}[k]}, \hat{p}^{\mathrm{DC}[k]}\right), \tag{15c}$$

for all $(\mathbf{A}^\delta, \mathbf{u}^\delta, \hat{p}^\delta) \in X \times Y(\mathbf{0}) \times Z$ for a particular iteration [k], which follows from the assumption that $(\delta_A^{\mathrm{DC}[k]}, \delta_u^{\mathrm{DC}[k]}, \delta_{\hat{p}}^{\mathrm{DC}[k]})$ are small.§ The solution updates $(\delta_A^{\mathrm{DC}[k]}, \delta_u^{\mathrm{DC}[k]}, \delta_{\hat{p}}^{\mathrm{DC}[k]})$ are used to obtain $\mathbf{A}^{DC[k+1]}$, $\mathbf{u}^{DC[k+1]}$ and $\hat{p}^{\mathrm{DC}[k+1]}$ in a similar way to (10). Once again, if the initial guess $(\mathbf{A}^{\mathrm{DC}[0]}, \mathbf{u}^{\mathrm{DC}[0]}, \hat{p}^{\mathrm{DC}[0]}) \in X \times Y(\mathbf{0}) \times Z$ is chosen to be sufficiently close to $(\mathbf{A}^{\mathrm{DC}}, \mathbf{u}^{\mathrm{DC}}, \hat{p}^{\mathrm{DC}}) \in (X \times Y(\mathbf{0}) \times Z)$, the iterates $(\mathbf{A}^{\mathrm{DC}[0]}, \mathbf{u}^{\mathrm{DC}[0]}, \hat{p}^{\mathrm{DC}[0]})$, $(\mathbf{A}^{\mathrm{DC}[1]}, \mathbf{u}^{\mathrm{DC}[1]}, \hat{p}^{\mathrm{DC}[1]})$, $(\mathbf{A}^{\mathrm{DC}[2]}, \mathbf{u}^{\mathrm{DC}[2]}, \hat{p}^{\mathrm{DC}[2]}), \cdots \in (X \times Y(\mathbf{0}) \times Z)$ are expected to converge to the continuous solutions $(\mathbf{A}^{\mathrm{DC}}, \mathbf{u}^{\mathrm{DC}}, \hat{p}^{\mathrm{DC}}) \in (X \times Y(\mathbf{0}) \times Z)$ of (5). This problem can also be formulated in terms of $\mathbf{q}^{\mathrm{DC}} := (\mathbf{A}^{\mathrm{DC}}, \mathbf{u}^{\mathrm{DC}}, \hat{p}^{\mathrm{DC}})$. Find $\delta_q^{\mathrm{DC}[k]} \in W(\mathbf{0})$ such that

$$K\left(\delta_q^{\mathrm{DC}[k]}, \mathbf{q}^\delta; \mathbf{q}^{\mathrm{DC}[k]}, \mathbf{0}\right) = -R_q\left(\mathbf{q}^\delta; \mathbf{q}^{\mathrm{DC}[k]}, \mathbf{0}, \mathbf{0}, \mathbf{J}^{\mathrm{DC}}\right), \tag{16}$$

for all $\mathbf{q}^\delta \in W(\mathbf{0})$ with $\mathbf{q}^{\mathrm{DC}[k+1]} = \mathbf{q}^{\mathrm{DC}[k]} + \delta_q^{\mathrm{DC}[k]}$.

AC-stage

For completeness, we also recast (7) to: Find $\delta_q(t) \equiv \mathbf{q}^{\mathrm{AC}}(t) \in \tilde{W}(\mathbf{0}, \mathbf{0})(0, T]$, such that

$$\tilde{M}\left((\delta_q)_{tt}, \mathbf{q}^\delta\right) + \tilde{C}\left((\delta_q)_t, \mathbf{q}^\delta\right) + \tilde{K}\left(\delta_q, \mathbf{q}^\delta\right) = -\tilde{R}_q\left(\mathbf{q}^\delta\right), \tag{17}$$

for all $\mathbf{q}^\delta \in W(\mathbf{0})$, which does not require iteration as it is linear in the unknown fields; hence, the reason we call it the *linearised approach*. The bilinear forms $\tilde{M}$, $\tilde{C}$ and $\tilde{K}$ are associated with the mass, damping and stiffness contributions in the *linearised approach*, and can be expressed in terms of the definitions in (13) as

$$\tilde{M}\left((\delta_q)_{tt}, \mathbf{q}^\delta\right) := M\left((\delta_q)_{tt}, \mathbf{q}^\delta\right), \tag{18a}$$

$$\tilde{C}\left((\delta_q)_t, \mathbf{q}^\delta\right) := C\left((\delta_q)_t, \mathbf{q}^\delta; \mathbf{q}^{\mathrm{DC}}\right), \tag{18b}$$

$$\tilde{K}\left(\delta_q, \mathbf{q}^\delta\right) := K\left(\delta_q, \mathbf{q}^\delta; \mathbf{q}^{\mathrm{DC}}, \mathbf{0}\right), \tag{18c}$$

$$\tilde{R}_q(\mathbf{q}^\delta) := R_q\left(\mathbf{q}^\delta; \mathbf{q}^{\mathrm{DC}}, \mathbf{0}, \mathbf{0}, \mathbf{J}^s\right). \tag{18d}$$

In this case the solution of (17) will contain only the transient alternating current (AC) component of the fields, and thus the complete description is $\mathbf{q}(t) = \mathbf{q}^{\mathrm{DC}} + \delta_q(t)$. The linear nature of this system also allows for it to be transformed to the frequency domain by the application of a Fourier transform, which was the approach followed in our other work.[13]

4 | DISCRETISATION OF THE SYSTEM

In this section, we describe the spatial and temporal discretisation of (11) for the *nonlinear approach* and (16,17) for the *linearised approach*. The eventual aim of this formulation is to handle fully coupled nonlinear problems, which, for the *nonlinear approach*, will employ an iterative procedure at each time step to fully resolve the solution while, for the

---

§The directional derivatives in (15) have been previously stated in our other work[13] and, in the following, we relate them to the explicit expressions in (13) to avoid repetition.

linearised approach, will involve a static iterative solve followed by a linear time integration without iteration. The presentation includes a brief description of the spatial discretisation using *hp*-finite elements, which result in a semidiscrete system of coupled second order ODEs. We then present the temporal discretisation of the system of equations to allow for solutions in the time domain and close the section by presenting a solution algorithm for the *nonlinear* and *linearised approaches*, which summarises the steps required once the problems are fully discretised.

4.1 | Spatial discretisation

The spatial discretisation of the linearised system of coupled acousto-magneto-mechanical equations in (16) and (17) is extensively covered in our other work[13] and the work of Bagwell[47] and the spatial discretisation of (11) is analogous. Hence, we only briefly summarise the approach. We limit ourselves to the treatment of idealised MRI scanners that are assumed to be rotationally symmetric in the azimuthal direction so that the problem is axisymmetric. Our domain then becomes the meridian plane $\Omega^m = \{(r, z) : 0 < r < \infty, -\infty < z < \infty\}$, the current sources have the form $\boldsymbol{J}^s = J^s_\phi(r, z)\boldsymbol{e}_\phi$, and the unknown fields are $\boldsymbol{A} = A_\phi(r, z)\boldsymbol{e}_\phi$, $\boldsymbol{u} = u_r(r, z)\boldsymbol{e}_r + u_z(r, z)\boldsymbol{e}_z$ and $\hat{p} = \hat{p}(r, z)$, where $\boldsymbol{e}_r, \boldsymbol{e}_\phi$, and $\boldsymbol{e}_z$ are the standard bases for the cylindrical coordinate system (r, z, ϕ). However, by projection of Ω^m the full 3-dimensional results are still achieved.

When transformed to the axisymmetric domain, the spaces in which the weak solutions are sought in the variational statements (11,16,17) must be adapted following the approach described in our other work[13] and the work of Bagwell.[47] To overcome the need for the solution in weighted spaces, to ensure the fields are well behaved at the radial axis, we transform the fields as $A_\phi = r\hat{A}_\phi$, $u_r = r\hat{u}_r$ and note that $\hat{A}_\phi \in H^1(\Omega^m)$ and $\tilde{\boldsymbol{u}} := [\hat{u}_r, u_z] \in (H^1(\Omega^m))^2$ and recall from our other work[13] that the acoustic pressure $\hat{p}(r, z) \in H^1(\Omega^m)$ presents no difficulty. The continuous update fields and test functions in the Newton-Raphson iterations are also treated in an analogous manner.

To achieve a finite computational domain, Ω^m is truncated by the introduction of infinite elements[48] for the far-field treatment of $\hat{A}_\phi$ and a perfectly matched layer approach[49] for the far-field treatment of $\hat{p}$. The far-field decay of the update fields is also treated analogously. For the details, we refer again to our other work[13] and the work of Bagwell.[47] Then, a nonoverlapping partition $(\mathcal{V}, \mathcal{E}, \mathcal{I})$ of Ω^m is achieved through the generation of a hybrid unstructured triangular-quadrilateral mesh, where $\mathcal{V}$ denotes the set of vertices, $\mathcal{E}$ the set of edges, and $\mathcal{I}$ the set of cells. In each element, we employ the H^1 conforming hierarchic finite element basis functions proposed by Schöberl and Zaglmayr,[50,51] which allow for arbitrary increases in element order p and local refinement of the mesh spacing h, for the spatial discretisation of the fields A_ϕ, $\tilde{\boldsymbol{u}}$, and $\hat{p}$ and the associated continuous update fields.

For a discretisation consisting of uniform order p elements, and a mesh consisting of $N_{\mathcal{V}}$ vertices, $N_{\mathcal{E}}$ edges, $N_{\mathcal{I}^T}$ triangular cells and $N_{\mathcal{I}^Q}$ quadrilateral cells, there will be $N = N_{\mathcal{V}} + (p-1)N_{\mathcal{E}} + \frac{1}{2}(p-2)(p-1)N_{\mathcal{I}^T} + (p-1)^2 N_{\mathcal{I}^Q}$ degrees of freedom for (each component of) each field.

4.1.1 | Nonlinear approach

Following a spatial discretisation using a uniform order approximation, the semidiscrete vector of updates and unknowns for problem (11) become

$$\boldsymbol{\delta}_{\text{q}}^{[k]}(t) = \left\{\begin{matrix} \boldsymbol{\delta}_{A_\phi} \\ \boldsymbol{\delta}_{\tilde{\boldsymbol{u}}} \\ \boldsymbol{\delta}_{\hat{p}} \end{matrix}\right\}^{[k]}(t) \in \mathbb{R}^{4N}, \qquad \boldsymbol{q}^{[k]}(t) = \left\{\begin{matrix} \boldsymbol{q}_{A_\phi} \\ \boldsymbol{q}_{\tilde{\boldsymbol{u}}} \\ \boldsymbol{q}_{\hat{p}} \end{matrix}\right\}^{[k]}(t) \in \mathbb{R}^{4N}, \qquad (19)$$

for each time t and the corresponding semidiscrete solution to the *nonlinear approach* reduces. Finding $\boldsymbol{\delta}_q^{[k]}(t)$ at each time $t \in (0, T]$ satisfying the following initial value problem:

$$\boldsymbol{M}\ddot{\boldsymbol{\delta}}_{\text{q}}^{[k]}(t) + \boldsymbol{C}^{[k]}\dot{\boldsymbol{\delta}}_{\text{q}}^{[k]}(t) + \boldsymbol{K}^{[k]}\boldsymbol{\delta}_{\text{q}}^{[k]}(t) = -\boldsymbol{R}_{\text{q}}^{[k]}, \qquad (20a)$$

$$\boldsymbol{q}^{[k+1]}(t) = \boldsymbol{q}^{[k]}(t) + \boldsymbol{\delta}_{\text{q}}^{[k]}(t), \qquad (20b)$$

$$\dot{\boldsymbol{q}}(0) = \boldsymbol{0}, \qquad (20c)$$

$$\boldsymbol{q}(0) = \boldsymbol{q}^{\text{DC}}, \qquad (20d)$$

where $\dot{\boldsymbol{\delta}}_{\text{q}}^{[k]} = d\boldsymbol{\delta}_{\text{q}}^{[k]}/dt$ and $\ddot{\boldsymbol{\delta}}_{\text{q}}^{[k]} = d^2\boldsymbol{\delta}_{\text{q}}^{[k]}/dt^2$. Equation (20) involves iteratively solving a second-order system of ODEs until $|\boldsymbol{R}_{\text{q}}^{[k]}| < \text{TOL}$ for some user-defined tolerance TOL. The convergence of $|\boldsymbol{R}_{\text{q}}^{[k]}|$ to 0 will be quadratic.[45] In the above,

$\mathbf{M}$, $\mathbf{C}^{[k]}$, $\mathbf{K}^{[k]}$, and $\mathbf{R}_q^{[k]}$ are the discrete linearised mass, damping and stiffness matrices, and residual vector, respectively, which are obtained by discretising the terms in (13) and depend, with the exception of the mass matrix, on the solution at iteration $[k]$. Explicit expressions for the matrices can be found in the work of Bagwell.[47] The vector $\mathbf{q}^{DC} \in \mathbb{R}^{4N}$ is the converged solution of (21) below.

4.1.2 | Linearised approach

DC-stage

In a similar manner, the *linearised approach* takes the form of a time-independent Newton-Raphson iteration. Find $\boldsymbol{\delta}_q^{DC[k]} \in \mathbb{R}^{4N}$ such that

$$\tilde{\mathbf{K}}\boldsymbol{\delta}_q^{\,DC[k]} = -\tilde{\mathbf{R}}_q^{DC[k]}, \tag{21a}$$

$$\mathbf{q}^{DC[k+1]} = \mathbf{q}^{DC[k]} + \boldsymbol{\delta}_q^{\,DC[k]}, \tag{21b}$$

$$\mathbf{q}^{DC[0]} = \mathbf{0}, \tag{21c}$$

with the iteration performed until $|\mathbf{R}_q^{DC[k]}| < \text{TOL}$, which follows from the discretisation of (16). The convergence of $|\mathbf{R}_q^{DC[k]}|$ to 0 will again be quadratic.

AC-stage

The *linearised approach* also requires the solution of the semidiscrete initial value problem. Find $\boldsymbol{\delta}_q^{[k]}(t) \in \mathbb{R}^{4N}$ at each time $t \in (0, T]$ such that

$$\tilde{\mathbf{M}}\ddot{\boldsymbol{\delta}}_q + \tilde{\mathbf{C}}\dot{\boldsymbol{\delta}}_q + \tilde{\mathbf{K}}\boldsymbol{\delta}_q = -\tilde{\mathbf{R}}_q, \tag{22a}$$

$$\boldsymbol{\delta}_q(0) = \dot{\boldsymbol{\delta}}_q(0) = \mathbf{0}, \tag{22b}$$

which follows from the discretisation of (17), where $\tilde{\mathbf{M}}$, $\tilde{\mathbf{C}}$, $\tilde{\mathbf{K}}$, and $\tilde{\mathbf{R}}_q$ are the discrete mass, damping and stiffness matrices, and the residual vector, respectively, obtained by discretising the terms in (18). Explicit expressions for the matrices can be found in the work of Bagwell.[47] The semidiscrete solution for the *linearised approach* is $\mathbf{q}(t) = \mathbf{q}^{DC} + \boldsymbol{\delta}_q(t)$.

4.2 | Temporal discretisation

There are a considerable number of alternative time integration techniques that could be employed for the temporal integration of (20) and (22), such as Euler schemes,[52] trapezoidal schemes,[53] and the Newmark method.[54] In this paper, we choose to adopt a second-order generalised-α scheme (see the work of Chung and Hulbert[55]) to discretise our system of equations. This scheme is designed to allow for tailor-made numerical dissipation in the solution and is of sufficient degree, given the second-order nature of (20) and (22). Given the complexity of the coupled system, it is difficult to know the true initial conditions for the full transient problem, when applying a forced excitation. The numerical dissipation of the generalised-α scheme is therefore beneficial as it can be used to damp out any artificial frequencies that pollute the solution. There exists also a number of high-order integration schemes, such as backward differentiation formulas,[56] explicit Runge-Kutta and leap-frog type methods,[57,58] that allow for higher-order accuracies in time and larger time steps, although with increased temporal accuracy comes a significant increase in computational cost. However, for our problem, the required time step size is dictated by the need to capture the excitation frequency and resonant frequencies of the system (typically in the region of 5000 Hz). For this reason, the need for higher-order accuracy is significantly outweighed by the requirement of smaller time step sizes anyway, and thus, the generalised-α scheme appears a sensible choice.

4.2.1 | Generalised-α time integration scheme (second order)

In this section, we focus on the development of the temporal discretisation of (20), which can similarly be developed for (22). The implicit form of this scheme evaluates the system of nonlinear equations in (20) at an intermediate time step $t_{n+1-\alpha_f}$ as

$$\mathbf{M}\ddot{\boldsymbol{\delta}}_{q\,n+1-\alpha_m}^{[k]} + \mathbf{C}|_{t_{n+1-\alpha_f}}^{[k]}\,\dot{\boldsymbol{\delta}}_{q\,n+1-\alpha_f}^{[k]} + \mathbf{K}|_{t_{n+1-\alpha_f}}^{[k]}\,\boldsymbol{\delta}_{q\,n+1-\alpha_f}^{[k]} = -\mathbf{R}_q|_{t_{n+1-\alpha_f}}^{[k]}, \tag{23}$$

where $\mathbf{C}|_{t_{n+1-\alpha_f}}^{[k]}$, $\mathbf{K}|_{t_{n+1-\alpha_f}}^{[k]}$, and $\mathbf{R}_q|_{t_{n+1-\alpha_f}}^{[k]}$ are evaluated at the intermediate time step $t_{n+1-\alpha_f}$ and the values of the fields at this time step are given by

$$\ddot{\mathbf{q}}_{n+1-\alpha_m}^{[k]} = (1 - \alpha_m)\ddot{\mathbf{q}}_{n+1}^{[k]} + \alpha_m\ddot{\mathbf{q}}_n, \tag{24a}$$

$$\dot{\mathbf{q}}_{n+1-\alpha_f}^{[k]} = (1 - \alpha_f)\dot{\mathbf{q}}_{n+1}^{[k]} + \alpha_f \dot{\mathbf{q}}_n, \tag{24b}$$

$$\mathbf{q}_{n+1-\alpha_f}^{[k]} = (1 - \alpha_f)\mathbf{q}_{n+1}^{[k]} + \alpha_f \mathbf{q}_n, \tag{24c}$$

$$t_{n+1-\alpha_f} = (1 - \alpha_f)t_{n+1} + \alpha_f t_n. \tag{24d}$$

The generalised-α scheme, described in the aforementioned work,[55] expresses $\mathbf{q}_{n+1}^{[k]}$ and $\dot{\mathbf{q}}_{n+1}^{[k]}$ in terms of $\ddot{\mathbf{q}}_{n+1}^{[k]}$, known as an acceleration-based formulation. This can be manipulated into a displacement based formulation, where $\dot{\mathbf{q}}_{n+1}^{[k]}$ and $\ddot{\mathbf{q}}_{n+1}^{[k]}$ are expressed in terms of $\mathbf{q}_{n+1}^{[k]}$, as

$$\ddot{\mathbf{q}}_{n+1}^{[k]} = \frac{1}{\beta}\left(\frac{\mathbf{q}_{n+1}^{[k]} - \mathbf{q}_n}{\Delta t^2} - \frac{\dot{\mathbf{q}}_n}{\Delta t} - \left(\frac{1}{2} - \beta\right)\ddot{\mathbf{q}}_n\right), \tag{25a}$$

$$\dot{\mathbf{q}}_{n+1}^{[k]} = \frac{\varsigma}{\beta}\left(\frac{\mathbf{q}_{n+1}^{[k]} - \mathbf{q}_n}{\Delta t} + \left(\frac{\beta}{\varsigma} - 1\right)\dot{\mathbf{q}}_n + \left(\frac{\beta}{\varsigma} - \frac{1}{2}\right)\Delta t\,\ddot{\mathbf{q}}_n\right), \tag{25b}$$

where $\varsigma := \frac{1}{2} - \alpha_m + \alpha_f$, $\beta := \frac{1}{4}(1 - \alpha_m + \alpha_f)^2$, $\alpha_m := \frac{2\rho_\infty - 1}{\rho_\infty + 1}$, $\alpha_f := \frac{\rho_\infty}{\rho_\infty + 1}$, Δt is the time step size and ρ_∞ denotes the user-specified value of the spectral radius in the high-frequency limit.[¶]

4.2.2 | Predictor-multi-corrector step

A predictor-corrector approach has been followed from the implementation standpoint.[59] The prediction step $[k = 0]$, based on a initial guess of the displacement field $\mathbf{q}_{n+1}^{[0]}$, is defined as

$$\ddot{\mathbf{q}}_{n+1}^{[0]} = \frac{1}{\beta}\left(\frac{\mathbf{q}_{n+1}^{[0]} - \mathbf{q}_n}{\Delta t^2} - \frac{\dot{\mathbf{q}}_n}{\Delta t} - \left(\frac{1}{2} - \beta\right)\ddot{\mathbf{q}}_n\right), \tag{26a}$$

$$\dot{\mathbf{q}}_{n+1}^{[0]} = \frac{\varsigma}{\beta}\left(\frac{\mathbf{q}_{n+1}^{[0]} - \mathbf{q}_n}{\Delta t} + \left(\frac{\beta}{\varsigma} - 1\right)\dot{\mathbf{q}}_n + \left(\frac{\beta}{\varsigma} - \frac{1}{2}\right)\Delta t\,\ddot{\mathbf{q}}_n\right), \tag{26b}$$

where (26a) and (26b) are consistent with (25a) and (25b), respectively. In other words both the velocity and accelerations predictors preserve second-order accuracy, as discussed in the work of Jansen et al.[60] If we return our attention to (25b) and (25a) and substitute the fields at iteration step $[k+1]$, we obtain that the update variables of the first- and second-order fields are

$$\delta_{\ddot{\mathbf{q}}\,n+1}^{[k]} = \frac{1}{\beta\Delta t^2}\delta_{\mathbf{q}\,n+1}^{[k]}, \tag{27a}$$

$$\delta_{\dot{\mathbf{q}}\,n+1}^{[k]} = \frac{\varsigma}{\beta\Delta t}\delta_{\mathbf{q}\,n+1}^{[k]}. \tag{27b}$$

4.2.3 | Fully discrete nonlinear approach

Using the relations between the updates, in (27), we may rewrite the discrete system, in (23), in terms of the update in the zeroth-order solution vector $\delta_{\mathbf{q}\,n+1}^{[k]}$ at time t_{n+1} as the following Newton-Raphson procedure. Find $\delta_{\mathbf{q}_{n+1}}^{[k]} \in \mathbb{R}^{4N}$ for $n = 0, 1, 2, \ldots, N_{\Delta t} = T/\Delta t$ such that

$$\left(\frac{(1 - \alpha_m)}{\beta\Delta t^2}\mathbf{M} + \frac{\varsigma(1 - \alpha_f)}{\beta\Delta t}\mathbf{C}|_{t_{n+1-\alpha_f}}^{[k]} + (1 - \alpha_f)\mathbf{K}|_{t_{n+1-\alpha_f}}^{[k]}\right)\delta_{\mathbf{q}\,n+1}^{[k]} = -\mathbf{R}_{\mathbf{q}}|_{t_{n+1-\alpha_f}}^{[k]}, \tag{28a}$$

$$\mathbf{q}_{n+1}^{[k+1]} = \mathbf{q}_{n+1}^{[k]} + \delta_{\mathbf{q}_{n+1}}^{[k]}, \tag{28b}$$

$$\dot{\mathbf{q}}_0 = \mathbf{0}, \tag{28c}$$

$$\mathbf{q}_0 = \mathbf{q}^{DC}, \tag{28d}$$

with the predictors (26) used to provide the initial guesses $\ddot{\mathbf{q}}_{n+1}^{[0]}$ and $\dot{\mathbf{q}}_{n+1}^{[0]}$, which are used to start the iteration over $[k]$ until $|\mathbf{R}_{\mathbf{q}}^{[k]}| < \text{TOL}$.

[¶]Traditionally with the generalised α method, γ is used to refer to the first stability parameter; however, given our formulation reserves γ for the material conductivity, we use instead the alternative symbol ς.

4.2.4 | Fully discrete linearised approach

AC-stage

The fully discrete version of (23) for the *linearised approach* is similarly expressed. Find $\boldsymbol{\delta}_{q\,n+1} \in \mathbb{R}^{4N}$ for $n = 0, 1, 2, \ldots, N_{\Delta t} = T/\Delta t$ such that

$$\left(\frac{(1 - \alpha_m)}{\beta \Delta t^2} \tilde{\mathbf{M}} + \frac{\varsigma(1 - \alpha_f)}{\beta \Delta t} \tilde{\mathbf{C}} + (1 - \alpha_f) \tilde{\mathbf{K}} \right) \boldsymbol{\delta}_{q\,n+1} = -\tilde{\mathbf{R}}_q|_{t_{n+1-\alpha_f}}, \tag{29a}$$

$$\dot{\boldsymbol{\delta}}_{q\,0} = \boldsymbol{\delta}_{q\,0} = \mathbf{0}, \tag{29b}$$

where the system matrices $\tilde{\mathbf{M}}$, $\tilde{\mathbf{C}}$, and $\tilde{\mathbf{K}}$ are independent of the previous temporal solutions, and $\tilde{\mathbf{R}}_q$ depends only on the evaluation of $\boldsymbol{J}^{AC}$ at time level $t_{n+1-\alpha_f}$ and so can be solved in a single step, which is a simplified version of (28).

4.3 | Solution algorithm

A general algorithm for computing the transient variation in the fields for both the *nonlinear* and *linearised approaches*, proposed above, under a generalised-α scheme is summarised in Algorithm 1. In the *nonlinear approach*, the algorithm involves 2 nested loops, the first over n performs the integration of the coupled system over time and, the second, over $[k]$ resolves the nonlinearity through the application of a Newton-Raphson iteration. In the *linearised approach*, this simplifies to a single loop over n to perform the time integration. Furthermore, Figure 4 summarises the steps required to construct the discretised Newton-Rapshon iterative scheme in (28) from the transient nonlinear transmission problem (1).

Algorithm 1 Algorithm to compute the time variation of the coupled transient system

---

1: Define the initial conditions of the fields $\mathbf{q}_0, \dot{\mathbf{q}}_0, \ddot{\mathbf{q}}_0$ from (3)

2: **for** $n = 0, 1, 2 \ldots N_{\Delta t}$ **do**   ▷ Number of timesteps $N_{\Delta t}$

3:      Predict the solution at the current timestep $\mathbf{q}_{n+1}^{[0]}, \dot{\mathbf{q}}_{n+1}^{[0]}, \ddot{\mathbf{q}}_{n+1}^{[0]}$ from (26)

4:      **while** $|\mathbf{R}_q| < \text{TOL}; \ k = 0, 1, 2 \ldots N_k$ **do**   ▷ Number of iterations N_k

5:          Compute the fields $\mathbf{q}_{n+1-\alpha_f}^{[k]}, \dot{\mathbf{q}}_{n+1-\alpha_f}^{[k]}$ and $\ddot{\mathbf{q}}_{n+1-\alpha_m}^{[k]}$ at $t_{n+1-\alpha_f}$ from (24)

6:          Solve the linear system (28) or (29a) for the solution update

$$\mathbf{K}_{TSM}^{[k]} \boldsymbol{\delta}_{q\,n+1}^{[k]} = -\mathbf{R}_q|_{t_{n+1-\alpha_f}}^{[k]},$$

         where $\mathbf{K}_{TSM}^{[k]} = \left(\frac{(1-\alpha_m)}{\beta \Delta t^2} \mathbf{M} + \frac{\varsigma(1-\alpha_f)}{\beta \Delta t} \mathbf{C}|_{t_{n+1-\alpha_f}}^{[k]} + (1 - \alpha_f) \mathbf{K}|_{t_{n+1-\alpha_f}}^{[k]} \right)$ for the *non linear approach* and $\mathbf{K}_{TSM} = \left(\frac{(1-\alpha_m)}{\beta \Delta t^2} \tilde{\mathbf{M}} + \frac{\varsigma(1-\alpha_f)}{\beta \Delta t} \tilde{\mathbf{C}} + (1 - \alpha_f) \tilde{\mathbf{K}} \right)$ and $\mathbf{R}_q$ is replaced by $\tilde{\mathbf{R}}_q$ for the *linearised approach*

7:          Update the solution fields

$$\mathbf{q}_{n+1}^{[k+1]} = \mathbf{q}_{n+1}^{[k]} + \boldsymbol{\delta}_{q\,n+1}^{[k]}$$

$$\dot{\mathbf{q}}_{n+1}^{[k+1]} = \dot{\mathbf{q}}_{n+1}^{[k]} + \frac{\varsigma}{\beta \Delta t} \boldsymbol{\delta}_{q\,n+1}^{[k]}$$

$$\ddot{\mathbf{q}}_{n+1}^{[k+1]} = \ddot{\mathbf{q}}_{n+1}^{[k]} + \frac{1}{\beta \Delta t^2} \boldsymbol{\delta}_{q\,n+1}^{[k]}$$

8:      **end while**

9: **end for**

---

5 | NUMERICAL EXAMPLES

In this section, we discuss two benchmark MRI test problems to justify that the conditions presented in Section 3.2 do hold in practice. We study the linearity of the fields for a range of different current density values in the coils to determine the validity of the *linearised approach*.
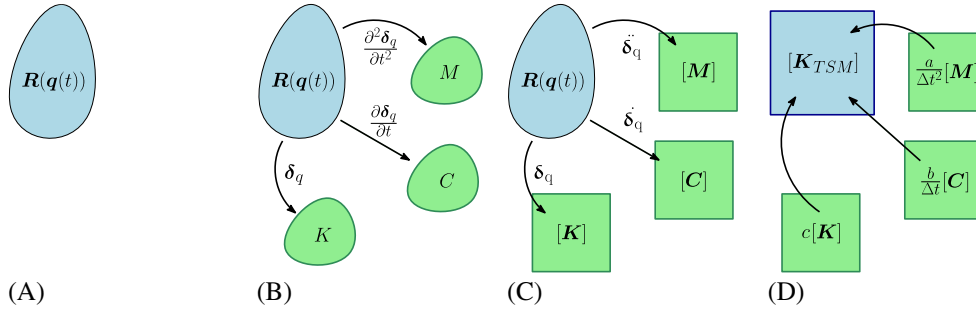
FIGURE 4 Summary of steps to solving transient nonlinear system. A, Residual weak form of coupled non-linear system; B, Linearisation of the nonlinear system; C, Discretisation of the directional derivatives; D, Temporal discretisation and building system matrix [Colour figure can be viewed at wileyonlinelibrary.com]
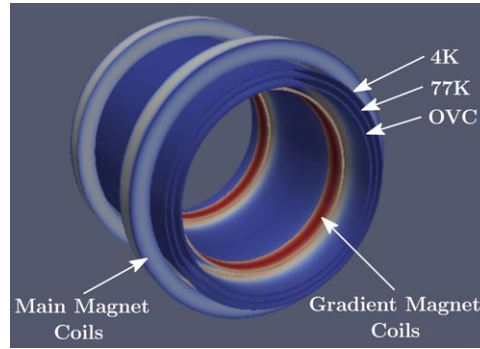
FIGURE 5 Test magnet problem: components of the simplified geometry. OVC, outer vacuum chamber [Colour figure can be viewed at wileyonlinelibrary.com]

5.1 | Test magnet problem

First, we consider solutions to the industrially relevant test magnet problem, which was previously presented in our other work[13] as the "Siemens benchmark problem." The conducting region Ω_c of the test magnet consists of three metallic shields, known as the outer vacuum chamber (OVC) Ω_c^{OVC}, $77°K$ radiation shield Ω_c^{77K}, and $4°K$ helium vessel Ω_c^{4K}, each with different material parameters (γ, μ, λ, G, ρ). The exact geometries and material parameters of the conducting components are commercially sensitive and as such are not displayed in this paper. By choosing to study only the Z-gradient coils and noting that the currents in the main coils and geometry of the conducting components are rotationally symmetric, the problem may be reduced to an axisymmetric description and solved in cylindrical coordinates (r, ϕ, z) on the meridian plane Ω^m. The full 3-dimensional representation of this simplified MRI scanner is depicted in Figure 5.

A pair of main magnet coils, each with a static current source $\boldsymbol{J}^{DC} = J_\phi^{DC}(r, z)\boldsymbol{e}_\phi$, are located on the outside of the three shields and a pair of Z-gradient magnet coils, each with alternating current source $\boldsymbol{J}^{AC}(t) = J_\phi^{AC}(t, r, z)\boldsymbol{e}_\phi$, are located within the imaging bore, both of which are assumed as Biot-Savart conductors and are located in free space. Realistic excitations of the gradient coil are nonsinusoidal in nature; however, for the purposes of comparison between the *linearised* and *nonlinear approaches*, we restrict ourselves to sinusoidal excitations, where the current density is described by $J_\phi^{AC}(t) = \text{Re}(|J_\phi^{AC}|e^{i\omega t})$. We consider several frequencies of excitation of $\omega = 2\pi[1000, 1500, 2000]\text{rad/s}$, which lie outside of the resonance region of $\omega \geq 2\pi[3500]$, predicted in our other works.[13,34] The magnitude of the static $|J_\phi^{DC}|$ and gradient current sources $|J_\phi^{AC}|$ to be considered are obtained from manufacturer's data.[6-8] This data quotes the maximum capable flux density on the central axis of the imaging bore ($r = 0$) and to obtain the corresponding current densities we have used the model described in Section 3.2.1, the results of which are summarised, for key clinical field strengths, in Table 1.

Given criteria 4) in Section 3.2, and hence the implication of the current density ratios, the greatest nonlinearity should appear for a magnet with the weakest static field of 1.5 T and the strongest gradient field of 100×10^{-3} T/m. This would result in a ratio between the static and gradient current density values of $|J_\phi^{AC}|/|J_\phi^{DC}| \approx 7.2\%$ for this problem. We therefore study the two *approaches* across a range of current density ratios of $|J_\phi^{AC}|/|J_\phi^{DC}| = [5, 10, 15, 20]\%$ to provide a rigourous test of the *linearised approach* for applications of higher levels of nonlinearity than current MRI scanners are capable of.

TABLE 1 Test magnet problem: typical values of the current densities in static and gradient coils and ranges of static and gradient field strengths from manufacturers data[6-8]

	Main Coil		Gradient Coil	
max $\left\|\boldsymbol{B}_{z=0}^{\mathrm{DC}}\right\|$[T]	$\left\|J_{\phi}^{\mathrm{DC}}\right\|$[$\times10^{-6}\mathrm{A/m^2}$]	max $\left\|\boldsymbol{B}_{z=0}^{\mathrm{AC}}\right\|$[$\times10^{-3}\mathrm{T/m}$]	$\left\|J_{\phi}^{\mathrm{AC}}\right\|$[$\times10^{-6}\mathrm{A/m^2}$]
1.5	218.35	30	4.70
3	436.70	80	12.53
11.7	1703.10	100	15.66

The problem is subject to the following boundary conditions: we fix the Dirichlet boundaries of the conductors to $\boldsymbol{u}^D = \boldsymbol{0}$ to fix the conductors in space, as in Section 2, and we set the value of the magnetic vector potential on the outer boundary to $A_\phi = 0$ due to the eddy current decay. The initial conditions of the problem are defined by (3).

We treat this problem computationally for both the *linearised* and *nonlinear approaches*. We truncate the nonconducting free-space region, comprised of air, and create the domain Ω^m, which is the same as in our other work.[13] In terms of spatial discretisation, we analyse the solution for a single unstructured mesh of 2842 triangles of maximum size $h = 0.25$ m, but with substantial refinement in the conductors Ω_c^m, resulting in 570 elements in Ω_c^m. The mesh parameters used are the same as in our other work[13]; however, due to improvements in the mesh generator used,[61] resulted in a better distribution of elements and hence fewer elements. We apply a single layer of 18 infinite (quadrilateral) elements on the outer boundary of Ω^m to resolve the static decay of the magnetic field, so that the boundary condition $A_\phi = 0$ is effectively imposed at infinity. We consider *p*-refinement for elements of order $p = [1, 2, 3, 4, 5]$. The temporal discretisation used to resolve these waves are studied for a time step size of $\Delta t = 2\pi/(\omega N_{\Delta t})$, where we vary the number of points per wavelength of the excitation frequency $N_{\Delta t} = [10, 20, 30, 40]$. The spectral radius of the α-scheme time integrator ρ_∞ allows for damping of certain frequency regimes. For $\rho_\infty = 1$ the amplitude of the wave is fully preserved and no damping of any high frequencies is introduced. For $\rho_\infty = 0$, the scheme is fully dissipative and higher frequency waves are completely damped; however, the damping of physical modes also occurs. Given that we wish to recover only physical modes in our problem, we therefore chose the value of $\rho_\infty = 0.8$, to allow for numerical damping of any nonphysical high frequencies induced through the forcing, whilst still preserving the physical lower frequency waves.

Solutions to this problem are obtained by applying Algorithm 1 for both the *nonlinear* and *linearised approaches* across the range of current densities and excitation frequencies discussed.

5.1.1 | Convergence study in outputs of interest

We consider quantities of industrial interest for both the mechanical and electromagnetic fields. For the electromagnetic field, we are concerned with the output power dissipation in the conducting components $P_{\Omega_c}^o$ and for the mechanical field we are concerned with the kinetic energy of the conducting components $E_{\Omega_c}^k$. The formal definition of these quantities in a full time-domain description, where the quantities are averaged over the time period T of excitation frequency, are

$$P_{\Omega_c}^o(t, \boldsymbol{A}) = \frac{1}{T}\int_t^{t+T}\int_{\Omega_c}\gamma|\boldsymbol{A}_t|^2\mathrm{d}\Omega\mathrm{d}t, \qquad E_{\Omega_c}^k(t, \boldsymbol{u}) = \frac{1}{T}\int_t^{t+T}\frac{1}{2}\int_{\Omega_c}\rho|\boldsymbol{u}_t|^2\mathrm{d}\Omega\mathrm{d}t, \tag{30}$$

which reduce, in a time harmonic representation, to

$$P_{\Omega_c}^o(\omega, \boldsymbol{A}) = \frac{1}{2}\int_\Omega\gamma\omega^2|\boldsymbol{A}(\omega)|^2\mathrm{d}\Omega, \qquad E_{\Omega_c}^k(\omega, \boldsymbol{u}) = \frac{1}{4}\int_\Omega\rho\omega^2|\boldsymbol{u}(\omega)|^2\mathrm{d}\Omega, \tag{31}$$

where $\boldsymbol{A}(\omega)$ and $\boldsymbol{u}(\omega)$ are the complex amplitudes of their respective fields as $\boldsymbol{A}(t) = \mathrm{Re}\,(\boldsymbol{A}(\omega)\,\mathrm{e}^{\mathrm{i}\omega t})$ and $\boldsymbol{u}(t) = \mathrm{Re}\,(\boldsymbol{u}(\omega)\,\mathrm{e}^{\mathrm{i}\omega t})$, as described in our other work.[13] To compute these quantities for the test magnet problem, using either the transient solutions obtained by the *linearised* or *nonlinear approaches*, Algorithm 1 is run at specific $N_{\Delta t}$, Δt, ρ_∞ for a sufficiently long time until the field responses reach steady state periodic solution. Equation (30) is approximated by Gaussian quadrature for the spatial integration (with sufficient quadrature points corresponding to the degree of the integrand) and a Trapezoidal rule for the temporal integration so that no further approximations are made.

In order to determine suitable spatial resolution in the solution, we perform a *p*-refinement study. We apply Algorithm 1 for $N_{\Delta t} = 30$, $\rho_\infty = 0.8$ using the *linearised approach* to compute the output power and kinetic energy across the frequency
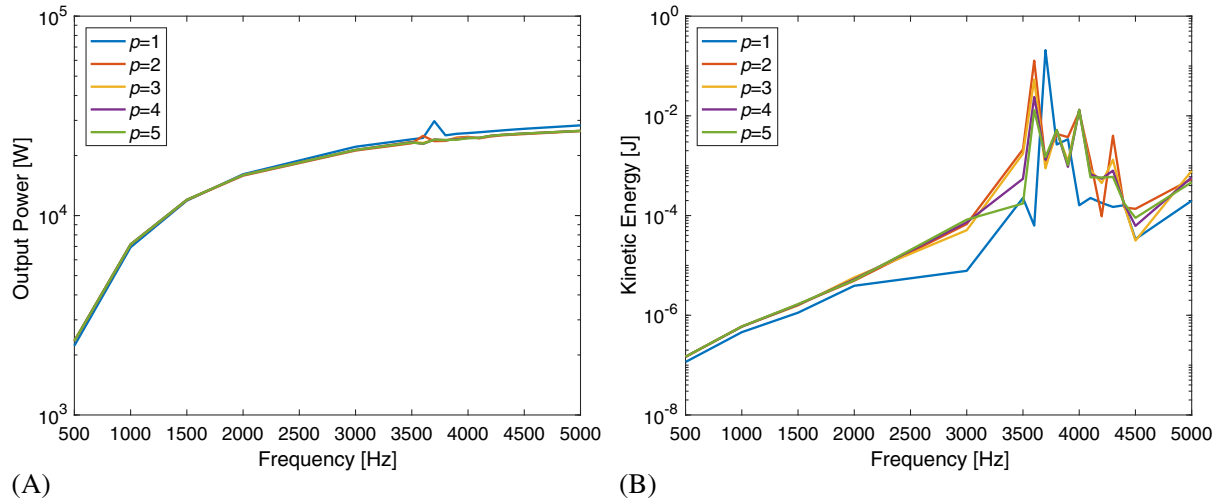
FIGURE 6 Test magnet problem. Results for element order $p = [1, 2, 3, 4, 5]$. A, Output power of the OVC (outer vacuum chamber); B, Kinetic energy of the OVC [Colour figure can be viewed at wileyonlinelibrary.com]

spectrum for $\omega \leq 2\pi[5000]$, the results of which are illustrated in Figure 6. For $p \leq 3$ the computed curves, illustrated in Figure 6, do not match one another and so the results have not yet reached convergence. The curves for $p = 4$ and $p = 5$, however, are practically indistinguishable for both the output power and kinetic energy and suggests that for elements of order $p = 4$ the results are sufficiently converged. We hence decide to adopt elements of $p = 4$ for all subsequent computations of this problem on the mesh specified previously.

A similar study to determine the required time step size was also carried out, where a range of number of time steps per wavelength $N_{\Delta t} = [10, 20, 30, 40]$ for $p = 4$ elements were studied. The results suggest that $N_{\Delta t} = 30$ offers sufficient temporal resolution to capture the amplitudes of the dominant frequency as well as frequencies twice the dominant frequency 2ω. The importance of this frequency doubling will be explained later in Section 5.1.3. Thus, for an excitation frequency of $\omega = 2\pi[1000]$, the time step size $\Delta t = 3.333 \times 10^{-5}s$, for $\omega = 2\pi[1500]$ the $\Delta t = 2.222 \times 10^{-5}s$ and for $\omega = 2\pi[2000]$ the $\Delta t = 1.667 \times 10^{-5}s$. For the full set of results, see our other work.[47]

Using these parameters, in Section 5.1.4, we compute the quantities in (30) by applying Algorithm 1 for the *linearised* and *nonlinear approaches* in the time domain and compare them with our previous frequency domain solver.[13] However, first we consider the results for the *linearised* and *nonlinear approaches* for transient electromagnetic and mechanical fields.

5.1.2 | Electromagnetic field

To perform comparisons between the *linearised* and *nonlinear approaches*, we compare the transient response of the magnetic field for both *approaches*. Given that the output power of the conductors $P_{\Omega_c}^o$, described above, is driven by the temporal derivative of the magnetic vector potential $\boldsymbol{A}_t$, we measure and compare the response of this field.

Figure 7 summarises the transient results of both *approaches* for the $\omega = 2\pi[2000]$rad/s sinusoidal excitation. The graphs in the left-hand column plot the time signal obtained from both the *linearised approach* (in red) and *nonlinear approach* (in black). The right hand column plots the corresponding frequency spectrum of the signal, obtained by performing fast Fourier transforms (FFTs). We can see from this figure that the *linearised approach* provides an accurate approximation of the magnetic vector potential across the full range of current density ratios. The relative norm of the difference in the time signals is 1.829×10^{-4} for $|J_\phi^{AC}|/|J_\phi^{DC}| = 5\%$ and 2.1888×10^{-4} for $|J_\phi^{AC}|/|J_\phi^{DC}| = 20\%$. The magnitude of the frequencies across the spectrum are almost identical and the *linearised approach* is even capable of capturing all the fundamental frequencies, around $\omega = 2\pi[3500 - 4000]$rad/s.

Figure 8 plots the transient response and corresponding frequency spectrum for a current density ratio of $|J_\phi^{AC}|/|J_\phi^{DC}| = 20\%$ and a range of excitation frequencies. These plots again illustrate the agreement between the *linearised* and *nonlinear approaches* for different excitation frequencies.
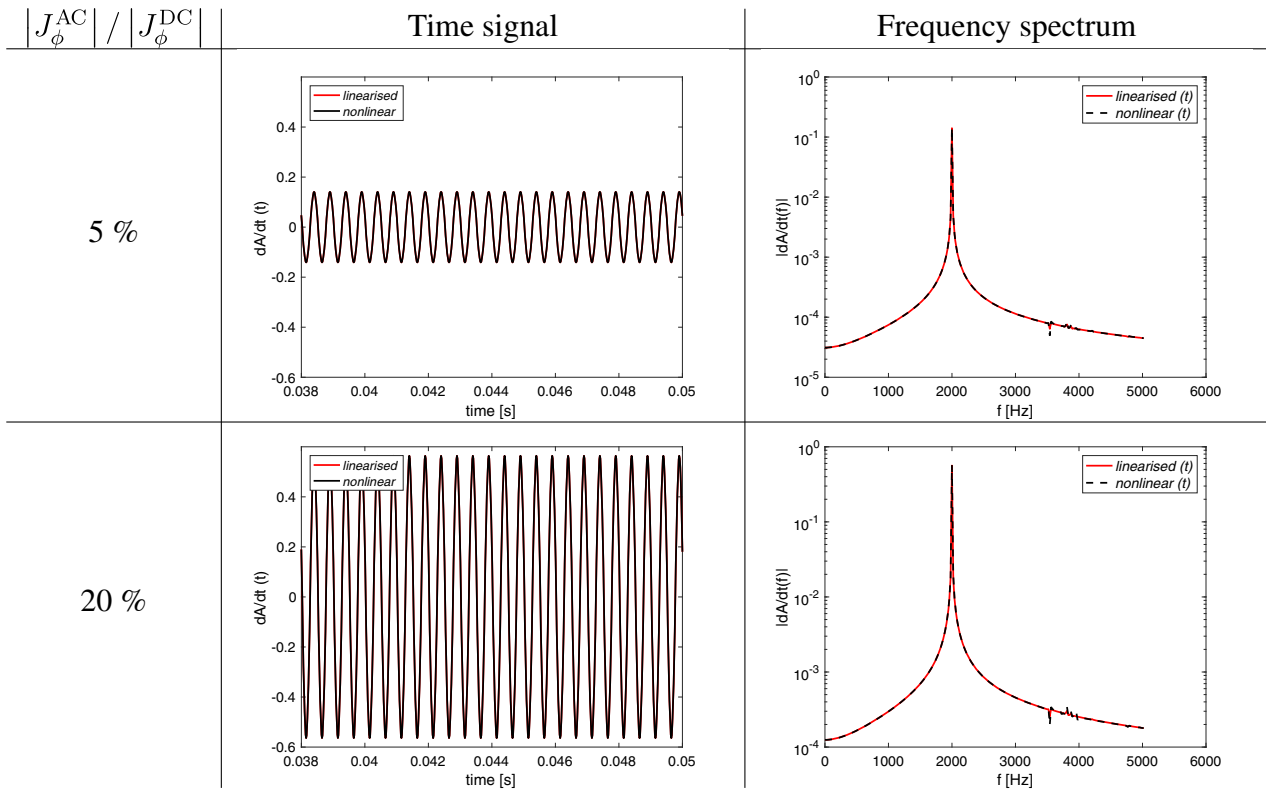
FIGURE 7 Test magnet problem. Time signals and corresponding fast Fourier transforms (FFTs) of A_t for both the *linearised* (red line) and *nonlinear approaches* (black line), for various values of $|J_\phi^{AC}|/|J_\phi^{DC}|$ subject to a $\omega = 2\pi[2000]$rad/s sinusoidal excitation [Colour figure can be viewed at wileyonlinelibrary.com]
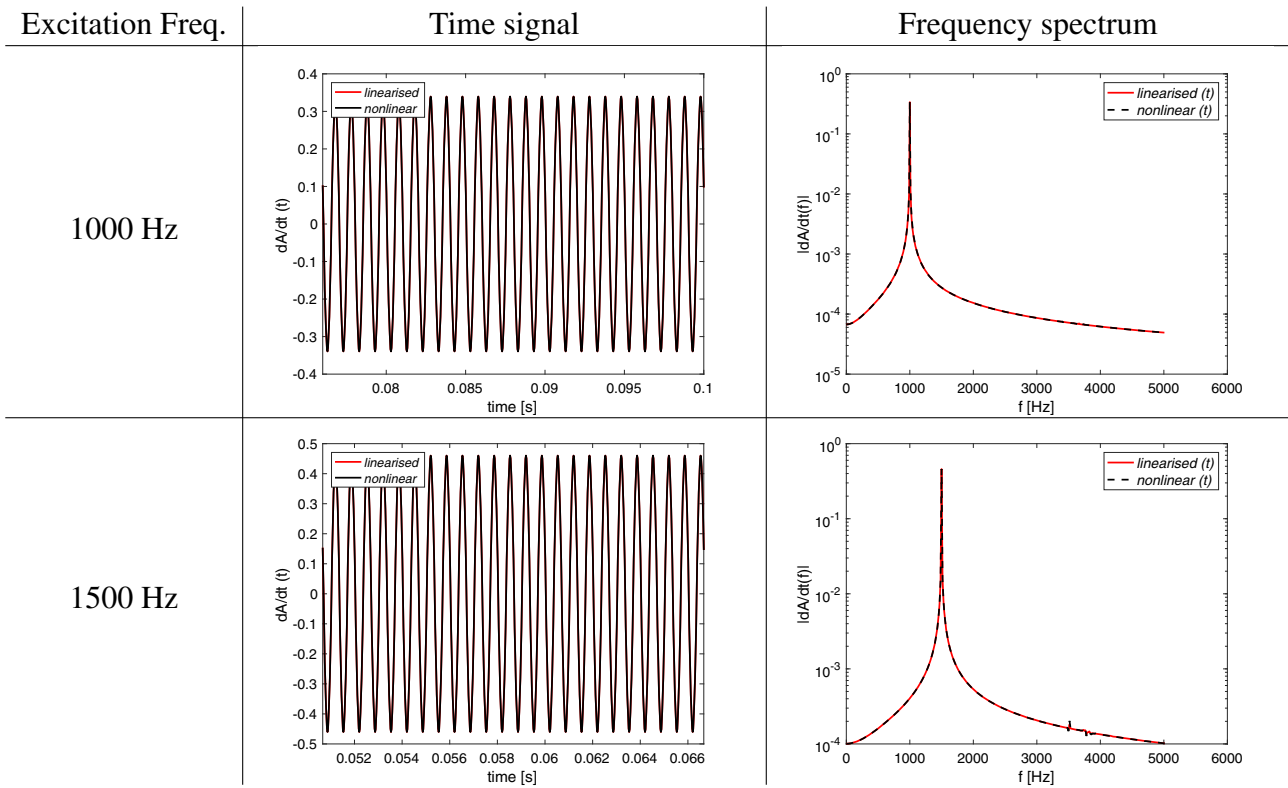
FIGURE 8 Test magnet problem. Time signals and corresponding fast Fourier transforms (FFTs) of A_t for both the *linearised* and *nonlinear approaches*, for $|J_\phi^{AC}|/|J_\phi^{DC}| = 20\%$ subject to various frequencies of excitation [Colour figure can be viewed at wileyonlinelibrary.com]
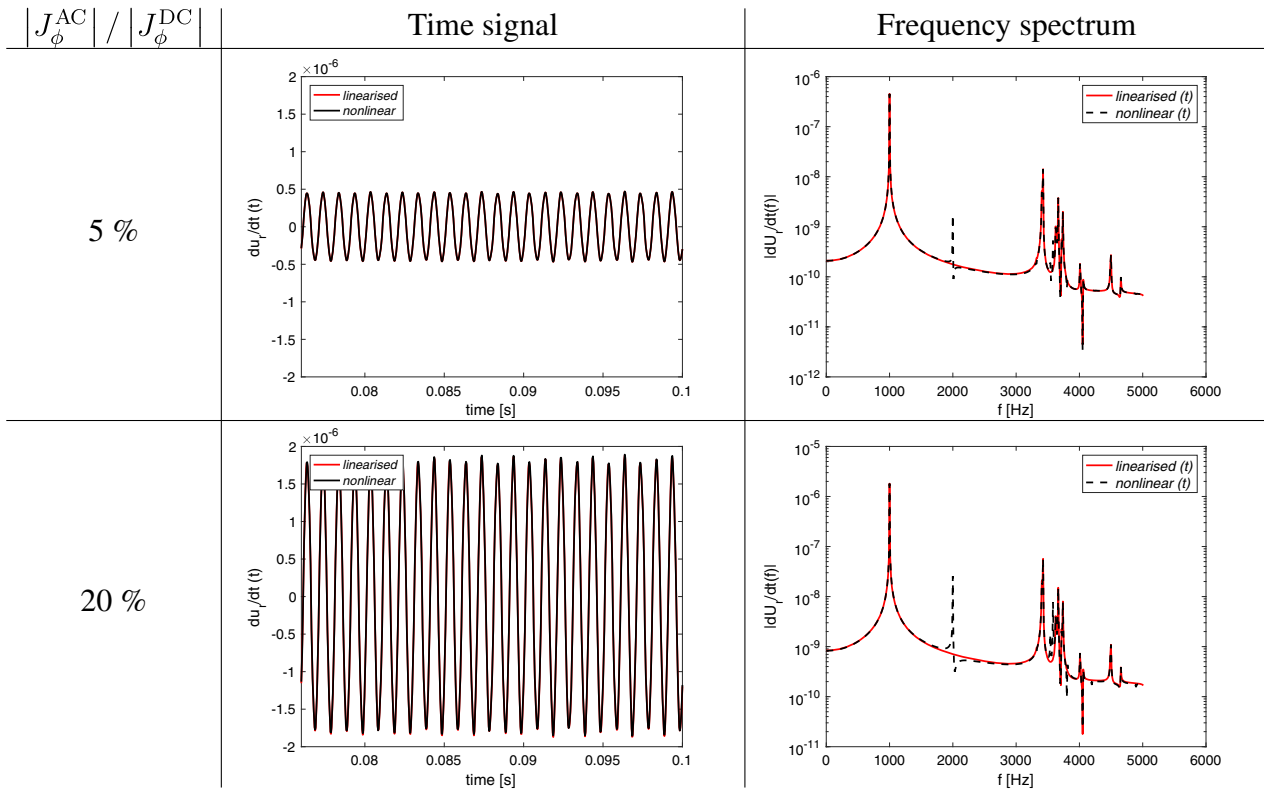
FIGURE 9 Test magnet problem. Time signals and corresponding fast Fourier transforms (FFTs) of $(u_r)_t$ for both the *linearised* and *nonlinear approaches*, for various values of $|J_\phi^{AC}|/|J_\phi^{DC}|$ subject to a $\omega = 2\pi[1000]$rad/s sinusoidal excitation [Colour figure can be viewed at wileyonlinelibrary.com]

5.1.3 | Mechanical field

We now compare the response of the mechanical field for both the *linearised* and *nonlinear approaches*. Given that the kinetic energy of the conductors $E_{\Omega_c}^k$, described in Section 5.1.1, is driven by their mechanical velocity $\boldsymbol{u}_t$, we measure and compare the response of this field.

Figure 9 summarises the transient results of both *approaches* for the $\omega = 2\pi[1000]$rad/s sinusoidal excitation. The graphs in the left-hand column plot the time signal obtained from both the *linearised approach* (in red) and *nonlinear approach* (in black). From the plots it appears as though the two *approaches* offer good agreement, especially when looking at the time signals. The relative norm of the differences between signals being 4.039×10^{-3} for $|J_\phi^{AC}|/|J_\phi^{DC}| = 5\%$ and 1.465×10^{-2} for $|J_\phi^{AC}|/|J_\phi^{DC}| = 20\%$. However, in the frequency spectrum there appears to be an extra frequency at $\omega = 2\pi[2000]$rad/s that is picked up in the *nonlinear approach*, but not in the *linearised approach*. This term appears due to the nonlinearity in the Maxwell stress tensor (2), which we can observe is quadratic in the magnetic field. From a decomposition of the magnetic field into static and dynamic components, as shown in Section 3.1.2, it can be shown that this nonlinear term comprises of a product of the dynamic component of the field with itself, which disappears in the *linearised approach*. This term causes a frequency doubling effect, in other words it results in a component of excitation of the mechanical field that is double the frequency of the AC currents. So for a $\omega = 2\pi[1000]$rad/s wave, as in Figure 10, an excitation at $\omega = 2\pi[2000]$rad/s would also appear, which matches exactly with the results obtained. However, from Figure 10, it is clear that the magnitude of this term is far smaller than that of the amplitude associated with the exciting frequency and thus has little effect on the solution. As the ratio of the current densities increases so too does the magnitude of this term. However, even for a ratio of 20% the magnitude is still several orders smaller than the main excitation and smaller also than the most dominant resonant frequencies. Thus the magnitude of this doubled frequency component provides a useful measure in determining the nonlinearity of the problem.

Figure 10 plots the transient response and corresponding frequency spectrum for a current density ratio of $|J_\phi^{AC}|/|J_\phi^{DC}| = 20\%$ and a range of excitation frequencies. We see from these plots that for the AC current frequencies of 1500 Hz, the agreement between the two *approaches* results in almost indistinguishable time signals. The relative norm of the differences between signals being 0.0349 for $\omega = 2\pi[1500]$rad/s and 0.0667 for $\omega = 2\pi[2000]$rad/s. However, for the

Excitation Freq.	Time signal	Frequency spectrum
1500 Hz		
2000 Hz		
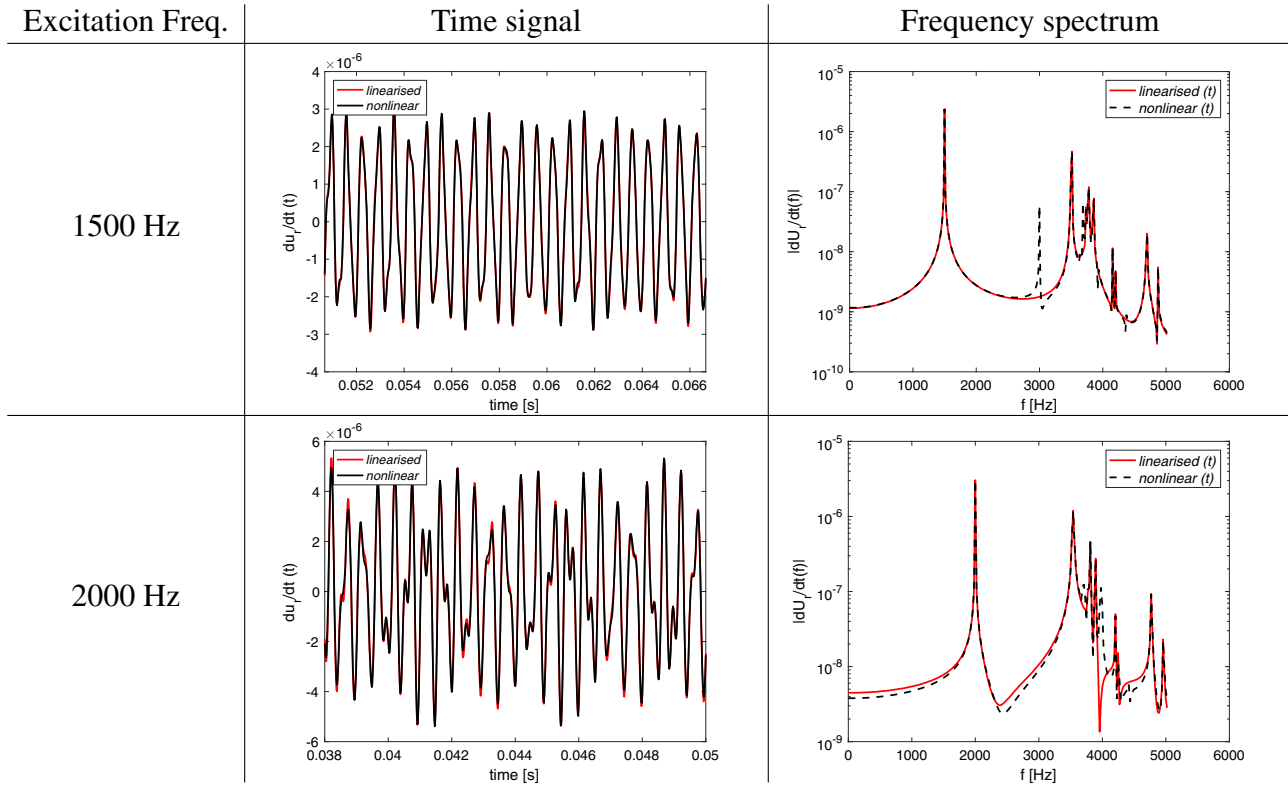
FIGURE 10 Test magnet problem. Time signals and corresponding fast Fourier transforms (FFTs) of $(u_r)_t$ for both the *linearised* and *nonlinear approaches*, for $|J_\phi^{AC}|/|J_\phi^{DC}| = 20\%$ subject to various frequencies of excitation [Colour figure can be viewed at wileyonlinelibrary.com]

$\omega = 2\pi[2000]$rad/s AC currents' differences in the time signal become more visible. This is because the doubled frequency excitation component of 4000 Hz lies within the resonance region. When exciting close to the resonance region, the problem results in matrices of high condition numbers, which are close to singular. Consequently, the tangent stiffness matrix inversion becomes more challenging and less reliable and, as a result, can lead to differences in the amplitudes across the frequency spectrum. Despite this effect however, the differences in the time signal are still very small and the characteristics of the system and prediction of the resonance region remain well captured by the *linearised approach*.

5.1.4 │ Comparison of *linearised* and *nonlinear approaches*

To benchmark the accuracy of the solution from the *linearised approach* with the *nonlinear approach*, we compare the computation of the outputs of interest for the two *approaches*, presented in Section 5.1.1, across the range of frequencies $\omega \leq 2\pi[5000]$rad/s. Figure 11 illustrates the outputs of interest computed by the *linearised approach* in both frequency and time domain and the *nonlinear approach* in time domain, using the definitions in (30) and (31) for a current density ratio of $|J_\phi^{AC}|/|J_\phi^{DC}| = 10\%$.

Using the frequency domain approach, described in our other work,[13] the outputs of interest $P^o_{\Omega_c}$ and $E^k_{\Omega_c}$ can be directly computed for a given excitation frequency. Whereas, in the time domain, we must run the time solver until steady state is obtained and then apply the definition in (30) across a time period. Due to the increased computational cost of computing the outputs of interest for transient solutions, we have chosen to compute them for a coarser frequency sweep compared with the frequency domain results. Figure 11A plots the output power in the OVC $P^o_{\Omega_c^{OVC}}(\omega, \boldsymbol{A}^{AC})$ and Figure 11B plots the kinetic energy in the OVC $E^k_{\Omega_c^{OVC}}(\omega, \boldsymbol{A}^{AC})$. For the results of the other shields, which show similar agreement, see our other work.[47] From the plots, the curves produced by the *linearised* and *nonlinear approaches* are almost indistinguishable across the frequency spectrum which suggests that the *linearised approach* provides a very accurate approximation to the full *nonlinear approach* across the full spectrum for $|J_\phi^{AC}|/|J_\phi^{DC}| = 10\%$ for the two outputs of interest. In fact, given that the individual fields, analysed in Sections 5.1.2 and 5.1.3, also show very good agreement for $|J_\phi^{AC}|/|J_\phi^{DC}| = 20\%$, we can hypothesise this to be the case also for the outputs of interest as they are directly related.
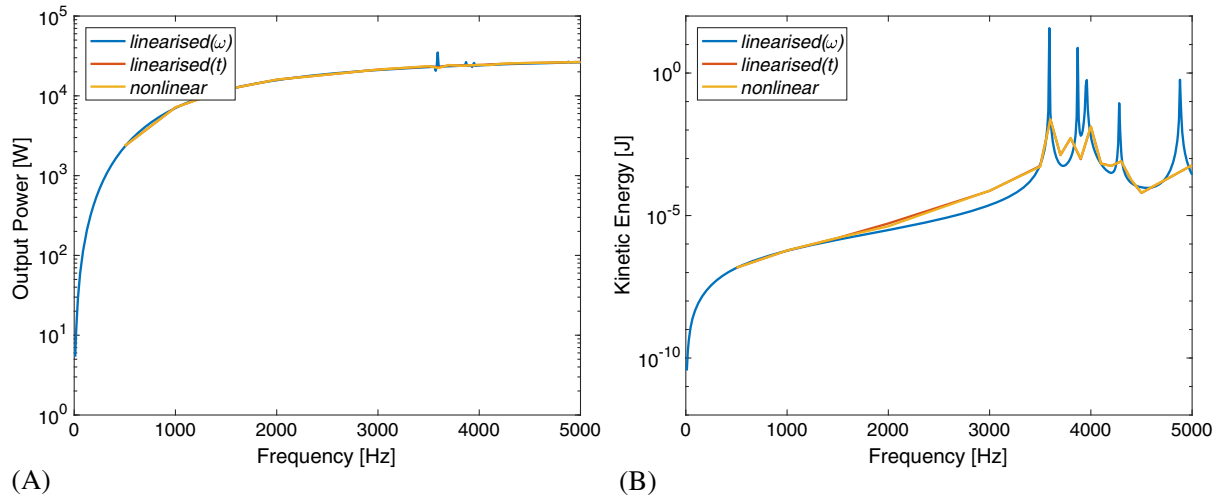
FIGURE 11 Test magnet problem. Results for the *linearised approach* in time and frequency domain as well as the *nonlinear approach*. A, Output power of the OVC (outer vacuum chamber); B, Kinetic energy of the OVC [Colour figure can be viewed at wileyonlinelibrary.com]
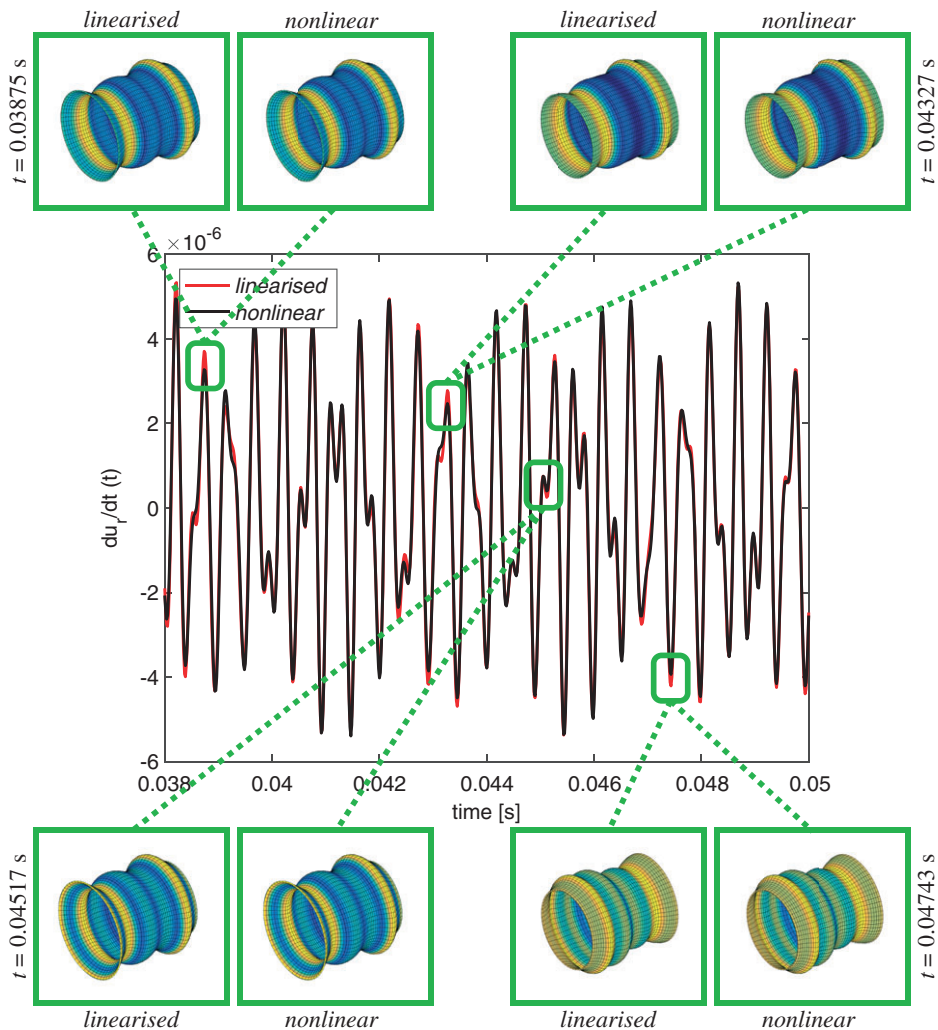
FIGURE 12 Test magnet problem. Comparison between the *linearised* and *nonlinear approaches* for displacements of the outer vacuum chamber (OVC) at different times for $|J_\phi^{AC}|/|J_\phi^{DC}| = 20\%$ and $\omega = 2\pi(2000)$rad/s [Colour figure can be viewed at wileyonlinelibrary.com]

TABLE 2 Test magnet problem: average computational times per time step of the *linearised* and *nonlinear approaches* for specific element order $p = [1, 2, 3, 4, 5]$

	Linearised Approach		Nonlinear Approach	
p	Computational time [s]	p	Computational time [s]	Speed-up
1	0.037	1	14.175	383
2	0.181	2	49. 327	273
3	0.489	3	116.830	239
4	1.150	4	206.424	179
5	2.187	5	358.914	164

We now compare the displacements of the mechanical shields by plotting the displacements of the OVC, in three dimensions, at interesting instances of the time signal for the radial velocity $(u_r)_t$ computed for the case of $|J_\phi^{AC}|/|J_\phi^{DC}| = 20\%$ and $\omega = 2\pi(2000)$rad/s in Figure 12. The chosen time instances across the time signal are plotted, where the difference in the mechanical velocities between the *linearised* and *nonlinear approaches* is noticeable. The contour plots of the displacement fields are all scaled such that the colour maps between the *linearised* and *nonlinear approaches* are the same. The displacements in Figure 12 are scaled by several orders of magnitude to show visually the displacement shapes of the shield. We can see that for all snapshots the differences between the two *approaches* are almost indistinguishable. This suggests that even for $J_\phi^{AC}|/|J_\phi^{DC}| = 20\%$ and an excitation frequency of $\omega = 2\pi(2000)$rad/s, where the doubled frequency component of $\omega = 2\pi(4000)$rad/s resides in the resonance region, see Section 5.1.3, that the *linearised approach* provides accurate and comparable results to the full *nonlinear approach*. For the results of the other shields, see our other work.[47]

The average computational timings, per time step, for the two *approaches* across a range of different element orders p are summarised in Table 2. The comparison between the computational timings of the two *approaches* suggests that the *linearised approach* is orders of magnitude more efficient in terms of computational cost than the *nonlinear approach*. For low-order $p = 1$ elements the *linearised approach* requires 383 times less computational effort than the *nonlinear approach*. Whereas, for higher-order $p = 5$ elements the *linearised approach* requires 164 times less computational effort than the *nonlinear approach*. This speed-up factor appears to offer an inverse exponential behaviour with p, which is due to the higher requirement on the solver for higher-order elements. Nevertheless, the computational timings displayed in the table suggest that the *linearised approach* offers orders of magnitude increase in computational efficiency over the *nonlinear approach*.

5.2 | Realistic magnet problem

We now consider a more realistic problem that represents, very accurately, the sorts of MRI scanner designs currently used in clinical operation. The geometry is illustrated in Figure 13A. This problem consists of a similar construction to the previous problem, where the conducting region is comprised of the three radiation shields $\Omega_c = \Omega_c^{OVC} \cup \Omega_c^{77K} \cup \Omega_c^{4K}$,

(A)   (B)
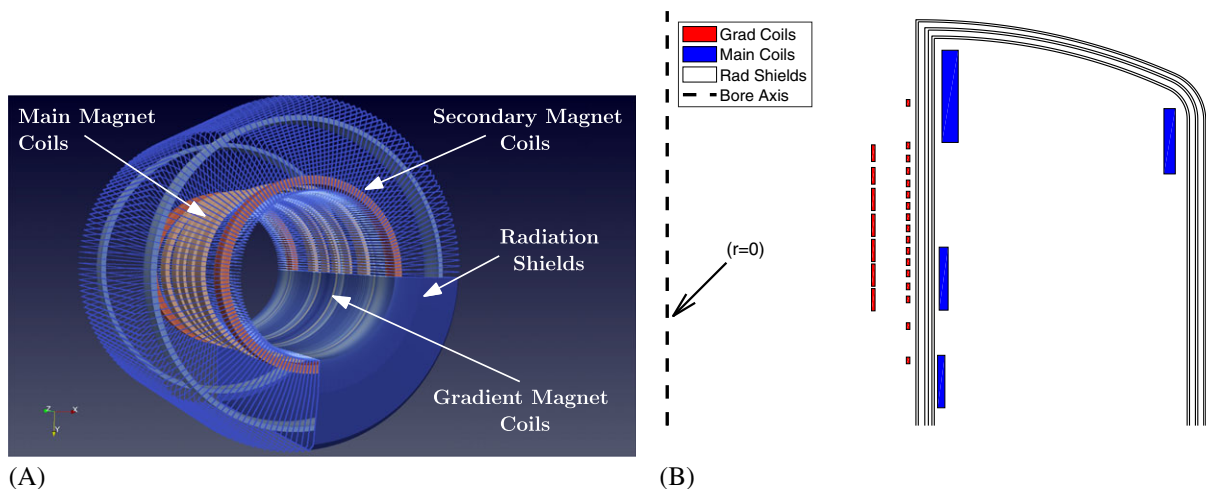
FIGURE 13 Realistic magnet problem: components of the simplified geometry. A, $\mathbb{R}^3$ domain, Ω; B, Positive Half Meridian domain, Ω^m [Colour figure can be viewed at wileyonlinelibrary.com]
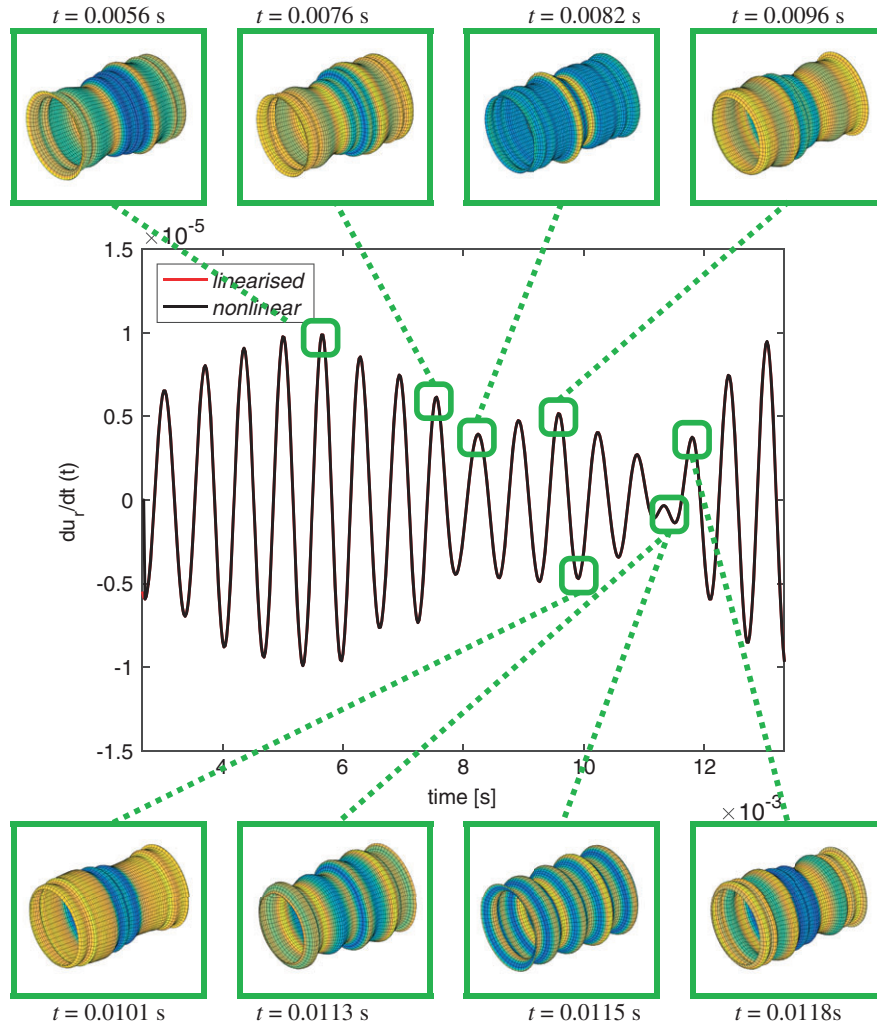
FIGURE 14 Full magnet problem. Displacements of the outer vacuum chamber (OVC) at different times for $|J_\phi^{AC}|/|J_\phi^{DC}| = 15\%$ and $\omega = 2\pi(1500)\text{rad/s}$ [Colour figure can be viewed at wileyonlinelibrary.com]

each with different material parameters (γ, μ, λ, G, ρ). The geometry of the radiation shields, however, is more complex and their topology represents that of closed cylindrical shells of trapezoidal cross section, with curved face end sections. However, despite the increased complexity in topology, the geometry is still cylindrical and can be treated as axisymmetric. Again, the exact geometries and material parameters of the conducting components are commercially sensitive and as such are not displayed in this paper. The configuration of the static main coil consists of the same block cross section as
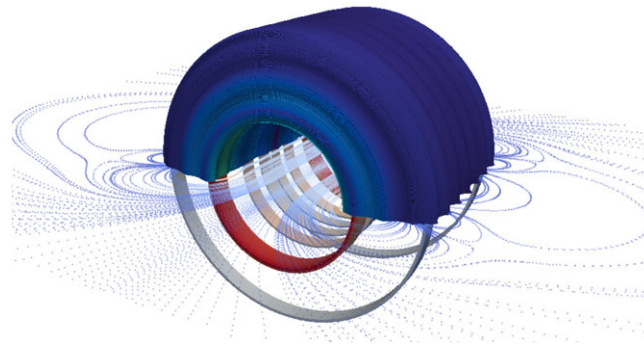
FIGURE 15 Full magnet problem. Distorted outer vacuum chamber (OVC), main coils, and corresponding static magnetic field lines for the static problem where $\boldsymbol{J}^s = \boldsymbol{J}^{DC}$ and $t = 0$ s [Colour figure can be viewed at wileyonlinelibrary.com]

the test magnet problem, but contains more sets of coils including also a set of secondary coils, which act to minimise the magnetic stray field by reversing the polarity of the magnetic field. The gradient coils of this problem represent a far more realistic Z-gradient coil structure, which also contains a set of primary and secondary coils for shielding. The coils

(A)

(B)

(C)

(D)

(E)

(F)

(G)

(H)
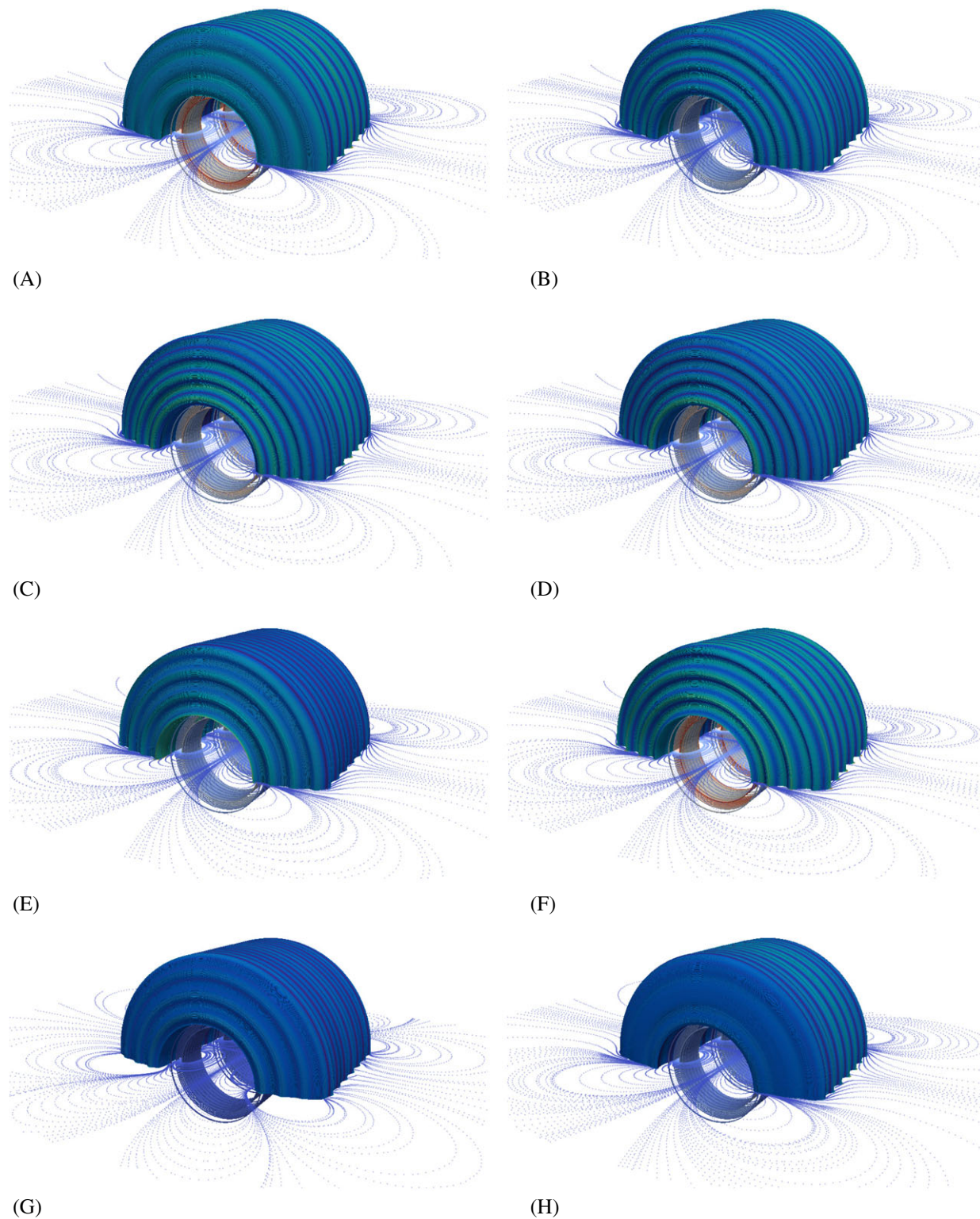
FIGURE 16 Full magnet problem. Snapshots of the distorted outer vacuum chamber (OVC), gradient coils and corresponding gradient magnetic field lines at various time intervals for $|J_\phi^{AC}|/|J_\phi^{DC}| = 15\%$ and $\omega = 2\pi(1500)$rad/s. A, $t = 0.0056$ s; B, $t = 0.0076$ s; C, $t = 0.0082$ s; D, $t = 0.0096$ s; E, $t = 0.0101$ s; F, $t = 0.0113$ s; G, $t = 0.0115$ s; H, $t = 0.0118$ s [Colour figure can be viewed at wileyonlinelibrary.com]

are sourced in the same way as the test magnet problem. The cross section of this problem, projected onto the positive half axisymmetric meridian domain $\Omega^m(r, z \geq 0)$, is illustrated in Figure 13B.

Given criteria 4) in Section 3.2, and hence the implication of the current density ratios, the greatest nonlinearity is expected to appear for a magnet with weakest static field of 1.5 T and strongest gradient field of 100×10^{-3} T/m. This would result in a ratio between the static and gradient current density values of $|J_\phi^{AC}|/|J_\phi^{DC}| \approx 12.3\%$ for this problem. We therefore study the two *approaches* for an extreme case of a current density ratio of $|J_\phi^{AC}|/|J_\phi^{DC}| = 15\%$ to rigorously test the *linearised approach*. The form of the excitation of J_ϕ^{AC} is as described in Section 5.1.

In terms of boundary conditions, we truncate the nonconducting free-space region, comprised of air, and create the domain Ω^m and apply those similar to the test magnet problem, whereby we set the Dirichlet boundaries of the conductors to $\boldsymbol{u}^D = \boldsymbol{0}$ to fix the conductors in space. We also set the magnetic vector potential to be $A_\phi = 0$ on the outer boundary.

In terms of spatial discretisation, we analyse the solution for an unstructured mesh of 19 218 triangles of maximum size $h = 0.25$ m, but with substantial refinement in the conductors Ω_c^m, resulting in 4085 elements in Ω_c^m. We then apply a single layer of 40 (quadrilateral) infinite elements on the outer boundary of Ω^m to resolve the static decay of the magnetic field. Having carried out similar convergence studies to those presented for the test magnet problem, we have chosen to use order $p = 4$ elements, $N_{\Delta t} = 30$ time steps per excitation frequency ω, and set $\rho_\infty = 0.8$ for the solutions to this problem.

We now compare the displacements of the mechanical shields by plotting the velocity magnitude of the system across the time signal using both *approaches* for $|J_\phi^{AC}|/|J_\phi^{DC}| = 15\%$ and $\omega = 2\pi(1500)$rad/s in Figure 14. Given that the differences in both the time signal and the displaced shapes of the OVC between the two *approaches* are almost indistinguishable, we highlight instead snapshots of the mechanical displacement in the inner OVC shell at various time instances across the time signal for the *linearised approach*. For the full results of the other shields (see our other work[47]). We plot the displaced OVC and static magnetic field for the static problem, in Figure 15, and the corresponding gradient fields, at various time instances, in Figure 16. The displacements in Figures 14, 15, and 16 are scaled by several orders of magnitude to show visually the displacement shapes of the OVC.

6 | CONCLUSION

In this paper, we have described a framework for both the *linearised* and *nonlinear approaches* to obtain transient solutions to the acousto-magneto-mechanical coupling in MRI scanners. We have demonstrated numerically that the *linearised approach* is in excellent agreement with the *nonlinear approach* and have estimated the energy present in the *nonlinear approach*, which is not captured by the *linearised approach*. In terms of the two questions we posed at the start of the paper, through the numerical examples presented in Section 5, we have shown that: (i) there is accurate agreement between the two *approaches* and that, not only does the *linearised approach* provide accurate approximations to the transient response of the fields, but also accurately predicts the quantities of interest and the resonance behaviour of MRI scanners, and (ii) the *linearised approach* provides accurate results across the full region of interest in the frequency spectrum $\omega \leq 2\pi[5000]$rad/s for a range of current density ratios $J_\phi^{AC}/J_\phi^{DC} \leq 20\%$ for a range of outputs of interest. In terms of current clinical MRI scanner applications, this ratio is restricted to around 4% to 12% and thus our analysis validates the use of the *linearised approach* in providing accurate solutions in current and future MRI scanner design, with orders of magnitude saving in the computational cost over the *nonlinear approach*.

ORCID

P.D. Ledger http://orcid.org/0000-0002-2587-7023

REFERENCES

1. Kozlowski P, Chang SD, Jones EC, Berean KW, Chen H, Goldenberg SL. Combined diffusion-weighted and dynamic contrast-enhanced MRI for prostate cancer diagnosis–correlation with biopsy and histopathology. *J Magn Reson Imaging*. 2006;24(1):108-113.

2. Brydie A, Raby N. Early MRI in the management of clinical scaphoid fracture. *Br J Radiol*. 2003;76(905):296-300.

3. Paty DW, Oger JJF, Kastrukoff LF, et al. MRI in the diagnosis of ms: a prospective study with comparison of clinical evaluation, evoked potentials, oligoclonal banding, and CT. *Neurology*. 1988;38(2):180.

4. Kirkham APS, Emberton M, Allen C. How good is MRI at detecting and characterising cancer within the prostate? *Eur Urol*. 2006;50(6):1163-1175.

5. Ahmed HU, Kirkham A, Arya M, et al. Is it time to consider a role for MRI before prostate biopsy? *Nat Rev Clin Oncol*. 2009;6(4):197-206.

6. Price D, Delakis I, Renaud C, Dickinson R. MRI scanners: A buyer's guide. https://pdfs.semanticscholar.org/df6b/bd32e99e1889bfcc61001285c6c96297e574.pdf. Accessed June 25, 2017.

7. Siemens. MAGNETOM family of MRI systems. http://www.deltamedicalsystems.com/DeltaMedicalSystems/media/Product-Details/MAGNETOM-Family-Brochure.pdf. Accessed June 25, 2017.

8. Siemens. Magnetic resonance imaging: The definitive portfolio for MRI. https://www.healthcare.siemens.com/magnetic-resonance-imaging?stc=wwhim800053. Accessed June 25, 2017.

9. van der Kolk AG, Hendrikse J, Zwanenburg JJM, Visser F, Luijten PR. Clinical applications of 7 T MRI in the brain. *Eur J Radiol*. 2013;82(5):708-718.

10. Kerchner GA. Ultra-high field 7T MRI: a new tool for studying alzheimer's disease. *J Alzheimer's Dis*. 2011;26(3):91-95.

11. Siemens. MAGNETOM Terra: Translate 7T research power into clinical care. https://www.healthcare.siemens.co.uk/magnetic-resonance-imaging/7t-mri-scanner/magnetom-terra. Accessed November 17, 2017.

12. Savage N. The world's most powerful MRI takes shape. http://spectrum.ieee.org/biomedical/imaging/the-worlds-most-powerful-mri-takes-shape. Accessed June 30, 2017.

13. Bagwell S, Ledger PD, Gil AJ, Mallett M, Kruip M. A linearised *hp*-finite element framework for acousto-magneto-mechanical coupling in axisymmetric MRI scanners. *Int J Numer Methods Eng*. 2017;112(10):1323-1352.

14. Cosmus TC, Parizh M. Advances in whole-body MRI magnets. *IEEE Trans Appl Supercond*. 2011;21(3):2104-2109.

15. Giovannetti G, Hartwig V, Viti V, etc. Low field elliptical MR coil array designed by FDTD. *Concepts Magn Reson Part B Magn Reson Eng*. 2008;33B(1):32-38.

16. Trakic A, Wang H, Liu F, Lopez HS, Crozier S. Analysis of transient eddy currents in MRI using a cylindrical FDTD method. *IEEE Trans Appl Supercond*. 2006;16(3):1924-1936.

17. Liu F, Crozier S. An FDTD model for calculation of gradient-induced eddy currents in MRI system. *IEEE Trans Appl Supercond*. 2004;14(3):1983-1989.

18. Zhao H, Crozier S, Liu F. Finite difference time domain (FDTD) method for modeling the effect of switched gradients on the human body in MRI. *Magn Reson Med*. 2002;48(6):1037-1042.

19. Liu F, Crozier S, Zhao H, Lawrence B. Finite-difference time-domain-based studies of MRI pulsed field gradient-induced eddy currents inside the human body. *Concepts Magn Reson*. 2002;15(1):26-36.

20. Liu F, Zhao H, Crozier S. Calculation of electric fields induced by body and head motion in high-field MRI. *J Magn Reson*. 2003;161(1):99-107.

21. Kozlov M, Turner R. Fast MRI coil analysis based on 3-D electromagnetic and RF circuit co-simulation. *J Magn Reson*. 2009;200(1):147-152.

22. Kroot JMB. Analysis of eddy currents in a gradient coil. *Sci Comput Electr Eng*. 2006;9:221-226.

23. Markiewicz DW, Vaghar MR, Dixon IR, Garmestani H. Generalized plane strain analysis of superconducting solenoids. *J Appl Phys*. 1999;86(12):7039-7051.

24. Li L, Cheng J, Cui C, et al. Numerical analysis of mechanical behavior for a 9.4-T whole-body MRI magnet. *IEEE Trans Appl Supercond*. 2017;27(4):1-5.

25. Chen J, Jiang X. Stress analysis of a 7 T actively shielded superconducting magnet for animal MRI. *IEEE Trans Appl Supercond*. 2012;22(3):4903104.

26. Dai Y, Wang C, Wang L, et al. Structural design of a 9.4 T whole-body MRI superconducting magnet. *IEEE Trans Appl Supercond*. 2012;22(3):4900404.

27. Shao W, Mechefske CK. Acoustic analysis of a gradient coil winding in an MRI scanner. *Concepts Magn Reson Part B Magn Reson Eng*. 2005;24(1):15-27.

28. Wang Y, Liu F, Crozier S. Simulation study of noise reduction methods for a split MRI system using a finite element method. *Med Phys*. 2015;42(12):7122-7131.

29. Wang Y, Liu F, Weber E, et al. Acoustic analysis for a split MRI system using FE method. *Concepts Magn Reson Part B Magn Reson Eng*. 2015;45(2):85-96.

30. Lin JC, Wang Z. Acoustic pressure waves induced in human heads by RF pulses from high-field MRI scanners. *Health Phys*. 2010;98(4):603-613.

31. Guan M, Wang X, Ma L, Zhou Y, Xin C. Magneto-mechanical coupling analysis of a superconducting solenoid magnet in self-magnetic field. *IEEE Trans Appl Supercond*. 2014;24(3):1-4.

32. Rausch M, Gebhardt M, Kaltenbacher M, Landes H. Magnetomechanical field computations of a clinical magnetic resonance imaging (MRI) scanner. *Int J Comput Math Electr Electron Eng (COMPEL)*. 2003;22(3):576-588.

33. Rausch M, Gebhardt M, Kaltenbacher M, Landes H. Computer-aided design of clinical magnetic resonance imaging scanners by coupled magnetomechanical-acoustic modeling. *IEEE Trans Magn*. 2005;41(1):72-81.

34. Ledger PD, Gil AJ, Poya R, Kruip M, Wilkinson I, Bagwell S. Solution of an industrially relevant coupled magneto-mechanical problem set on an axisymmetric domain. *Appl Math Model*. 2016;40(3):1959-1971.

35. Demkowicz L. *Computing with hp-adaptive Finite Elements: Volume 1 One and Two Dimensional Elliptic and Maxwell Problems*. Boca Raton, FL: Chapman and Hall/CRC; 2006.

36. Szabó B, Babuška IM. *Finite Element Analysis*. New York, NY: John Wiley and Sons; 1991.

37. Wheeler HA. Formulas for the skin effect. *Proc IRE*. 1942;30(9):412-424.

38. Gil AJ, Bonet J. Finite element analysis of prestressed structural membranes. *Finite Elem Anal Des*. 2006;42(8-9):683-697.

39. Gil AJ. Structural analysis of prestressed Saint Venant-Kirchhoff hyperelastic membranes subjected to moderate strains. *Comput Struct*. 2006;84(15-16):1012-1028.

40. Gil AJ, Bonet J. Finite element analysis of partly wrinkled reinforced prestressed membranes. *Comput Mech*. 2007;40(3):595-615.

41. Poya R, Sevilla R, Gil AJ. A unified approach for a posteriori high-order curved mesh generation using solid mechanics. *Comput Mech*. 2016;58(3):457-490.

42. Baek S, Gleason RL, Rajagopal KR, Humphrey JD. Theory of small on large: potential utility in computations of fluid-solid interactions in arteries. *Comput Methods Appl Mech Eng*. 2007;196(31-32):3070-3078.

43. Sprawls P. *Magnetic Resonance Imaging: Principles, Methods, and Techniques*. Madison, WI: Medical Physics Publishing; 2000.

44. Monk P. *Finite Element Methods for Maxwell's Equations*. New York, NY: Oxford University Press; 2003.

45. Bonet J, Gil AJ, Wood RD. *Nonlinear Solid Mechanics for Finite Element Analysis: Statics*. Cambridge, UK: Cambridge University Press; 2016.

46. Griffiths DJ. *Introduction to Electrodynamics*. London, UK: Pearson Education; 2014.

47. Bagwell S. A Numerical Multi-Physics Approach to Understanding MRI Scanners and Their Complex Behaviour [PhD thesis]. Swansea, UK: Swansea University; 2018.

48. Bettess P. *Infinite Elements*. Sunderland, UK: Penshaw Press; 1992.

49. Michler C, Demkowicz L, Kurtz J, Pardo D. Improving the performance of perfectly matched layers by means of *hp*-adaptivity. *Numer Methods Partial Differ Equ*. 2007;23(4):832-858.

50. Zaglmayr S. High order finite element methods for electromagnetic field computation [PhD thesis]. Linz, Austria: Johannes Kepler Univerität Linz; 2006.

51. Schöberl J, Zaglmayr S. High order Nédélec elements with local complete sequence properties. *Int J Comput Math Electr Electron Eng (COMPEL)*. 2005;24(2):374-384.

52. Liu T, Zhao C, Li Q, Zhang L. An efficient backward Euler time-integration method for nonlinear dynamic analysis of structures. *Comput Struct*. 2012;106:20-28.

53. Roache PJ, Dietrich DE. Evaluation of the filtered leapfrog-trapezoidal time integration method. *Numer Heat Transf*. 1988;14(2):149-164.

54. Artuzi WA. Improving the Newmark time integration scheme in finite element time domain methods. *IEEE Microw Wirel Compon Lett*. 2005;15(12):898-900.

55. Chung J, Hulbert GM. A time integration algorithm for structural dynamics with improved numerical dissipation: the generalized-α method. *J Appl Mech*. 1993;60(2):371-375.

56. Brayton RK, Gustavson FG, Hachtel GD. A new efficient algorithm for solving differential-algebraic systems using implicit backward differentiation formulas. *Proc IEEE*. 1972;60(1):98-108.

57. van Zuijlen AH, Bijl H. Implicit and explicit higher order time integration schemes for structural dynamics and fluid-structure interaction computations. *Comput Struct*. 2005;83(2-3):93-105.

58. Spachmann H, Schuhmann R, Weiland T. Higher order explicit time integration schemes for Maxwell's equations. *Int J Numer Model Electron Netw Devices Fields*. 2002;15(5-6):419-437.

59. Brooks AN, Hughes TJR. Streamline upwind/Petrov-Galerkin formulations for convection dominated flows with particular emphasis on the incompressible Navier-Stokes equations. *Comput Methods Appl Mech Eng*. 1982;32(1-3):199-259.

60. Jansen KE, Whiting CH, Hulbert GM. A generalized-α method for integrating the filtered Navier-Stokes equations with a stabilized finite element method. *Comput Methods Appl Mech Eng*. 2000;190(3-4):305-319.

61. Engwirda D. MESH2D-Delaunay-based unstructured mesh-generation. https://uk.mathworks.com/matlabcentral/fileexchange/25555-mesh2d-delaunay-based-unstructured-mesh-generation. Accessed September 18, 2017.

APPENDIX : ESTIMATES OF THE ENERGY NOT CAPTURED BY THE LINEARISED APPROACH

We investigate the energy in the *nonlinear approach* that is not captured by the *linearised approach*. To do this, we choose as solutions and weights $A = A^\delta = A^{\mathrm{DC}} + A^{\mathrm{AC}}$, $u = u^\delta = u^{\mathrm{DC}} + u^{\mathrm{AC}}$ and $\hat{p} = \hat{p}^\delta = \hat{p}^{\mathrm{DC}} + \hat{p}^{\mathrm{AC}}$ in (4). By doing so, the residuals

$$R_A\left(A^{\mathrm{DC}} + A^{\mathrm{AC}};\ A^{\mathrm{DC}} + A^{\mathrm{AC}}, u^{\mathrm{DC}} + u^{\mathrm{AC}}, J^{\mathrm{DC}} + J^{\mathrm{AC}}\right) \neq 0, \tag{A1a}$$

$$R_u\left(u^{\mathrm{DC}} + u^{\mathrm{AC}};\ A^{\mathrm{DC}} + A^{\mathrm{AC}}, u^{\mathrm{DC}} + u^{\mathrm{AC}}, \hat{p}^{\mathrm{DC}} + \hat{p}^{\mathrm{AC}}\right) \neq 0, \tag{A1b}$$

$$R_{\hat{p}}\left(\hat{p}^{\mathrm{DC}} + \hat{p}^{\mathrm{AC}};\ A^{\mathrm{DC}} + A^{\mathrm{AC}}, u^{\mathrm{DC}} + u^{\mathrm{AC}}, \hat{p}^{\mathrm{DC}} + \hat{p}^{\mathrm{AC}}\right) \neq 0, \tag{A1c}$$

represent the energy present in the *nonlinear approach* at each time t for the aforementioned choice of solution. An analogous procedure can be used to determine the energy captured by the *linearised approach* at each time t when using (5) and (6). Subtraction of the latter and (A1) leads to the energy not captured by the *linearised approach* when $A = A^\delta = A^{\mathrm{DC}} + A^{\mathrm{AC}}$, $u = u^\delta = u^{\mathrm{DC}} + u^{\mathrm{AC}}$ and $\hat{p} = \hat{p}^\delta = \hat{p}^{\mathrm{DC}} + \hat{p}^{\mathrm{AC}}$, namely

$$R_A(t) = -\int_{\Omega_c} \left(\gamma(u^{\mathrm{AC}})_t \times (\nabla \times A^{\mathrm{AC}}) \cdot (A^{\mathrm{DC}} + A^{\mathrm{AC}})\right) \mathrm{d}\Omega, \tag{A2a}$$

$$R_u(t) = \int_{\Omega_c} \left(\sigma^e(A^{\mathrm{AC}}) : \nabla(u^{\mathrm{DC}} + u^{\mathrm{AC}})\right) \mathrm{d}\Omega - \int_{\partial\Omega_c^N} \left((u^{\mathrm{DC}} + u^{\mathrm{AC}}) \cdot \sigma^e(A^{\mathrm{AC}})\big|_{\partial\Omega_c}^+ \, n\right) \mathrm{d}S, \tag{A2b}$$

$$R_{\hat{p}}(t) = -\int_{\mathrm{supp}(J^{\mathrm{AC}})} \left(((\nabla \times A^{\mathrm{AC}}) \times J^{\mathrm{AC}}) \cdot \nabla(\hat{p}^{\mathrm{DC}} + \hat{p}^{\mathrm{AC}})\right) \mathrm{d}\Omega. \tag{A2c}$$

Applying the Cauchy-Schwartz inequality to each of these expressions, in turn, we find the following.

R_A term

$$|R_A(t)| \leq \left\|\gamma(u^{\mathrm{AC}})_t\right\|_{L^2(\Omega_c)} \|\nabla \times A^{\mathrm{AC}}\|_{L^2(\Omega_c)} \left(\|A^{\mathrm{DC}}\|_{L^2(\Omega_c)} + \|A^{\mathrm{AC}}\|_{L^2(\Omega_c)}\right), \tag{A3}$$

where $\|u\|_{L^2(\Omega_c)}^2 := \int_{\Omega_c} |u|^2 \mathrm{d}\Omega$. It can be shown[44]

$$\|A^{\mathrm{DC}}\|_{L^2(\Omega_c)} \leq C\|\nabla \times A^{\mathrm{DC}}\|_{L^2(\Omega_c)}, \quad \|A^{\mathrm{AC}}\|_{L^2(\Omega_c)} \leq C\|\nabla \times A^{\mathrm{AC}}\|_{L^2(\Omega_c)} \tag{A4}$$

and $\|\cdot\|_{L^2(\Omega_c)} \leq |\Omega_c|\|\cdot\|_{L^\infty(\Omega_c)}$ is well known, where $|\Omega_c|$ defines the size of the domain Ω_c and $\|u\|_{L^\infty(\Omega_c)} = \sup_{x\in\Omega_c}|u(x)|$. Thus, combining with (A3) and (A4) gives

$$|R_A(t)| \leq C\left\|\gamma(u^{\mathrm{AC}})_t\right\|_{L^\infty(\Omega_c)} \|\nabla \times A^{\mathrm{AC}}\|_{L^\infty(\Omega_c)} \left(\|\nabla \times A^{\mathrm{DC}}\|_{L^\infty(\Omega_c)} + \|\nabla \times A^{\mathrm{AC}}\|_{L^\infty(\Omega_c)}\right). \tag{A5}$$

Provided that $\|\nabla \times A^{\mathrm{AC}}\|_{L^\infty(\Omega_c)} \ll \|\nabla \times A^{\mathrm{DC}}\|_{L^\infty(\Omega_c)}$ for all time t, or equivalently $\|B^{\mathrm{AC}}(t)\|_{L^\infty(\Omega_c)} \ll \|B^{\mathrm{DC}}\|_{L^\infty(\Omega_c)}$, we find

$$|R_A(t)| \leq C\left\|\gamma(u^{\mathrm{AC}})_t\right\|_{L^\infty(\Omega_c)} \|B^{\mathrm{DC}}\|_{L^\infty(\Omega_c)}^2, \tag{A6}$$

where C depends on the size of the domain Ω_c.

R_u term

Following similar steps to above we find that

$$\begin{aligned}
|R_u(t)| &\leq \|\nabla \times A^{\mathrm{AC}}\|_{L^2(\Omega_c)}^2 \left(\|\nabla u^{\mathrm{DC}}\|_{L^2(\Omega_c)} + \|\nabla u^{\mathrm{AC}}\|_{L^2(\Omega_c)}\right) \\
&\quad + \|\nabla \times A^{\mathrm{AC}}\|_{L^2(\partial\Omega_c^N)}^2 \left(\|u^{\mathrm{DC}}\|_{L^2(\partial\Omega_c^N)} + \|u^{\mathrm{AC}}\|_{L^2(\partial\Omega_c^N)}\right) \\
&\leq C\left(\|\nabla \times A^{\mathrm{AC}}\|_{L^\infty(\Omega_c)}^2 \left(\|\nabla u^{\mathrm{DC}}\|_{L^\infty(\Omega_c)} + \|\nabla u^{\mathrm{AC}}\|_{L^\infty(\Omega_c)}\right)\right. \\
&\quad \left. + \|\nabla \times A^{\mathrm{AC}}\|_{L^\infty(\partial\Omega_c^N)}^2 \left(\|u^{\mathrm{DC}}\|_{L^\infty(\partial\Omega_c^N)} + \|u^{\mathrm{AC}}\|_{L^\infty(\partial\Omega_c^N)}\right)\right) \\
&\leq C\left(\|B^{\mathrm{AC}}\|_{L^\infty(\Omega_c)}^2 \left(\|\nabla u^{\mathrm{DC}}\|_{L^\infty(\Omega_c)} + \|\nabla u^{\mathrm{AC}}\|_{L^\infty(\Omega_c)}\right)\right. \\
&\quad \left. + \|B^{\mathrm{AC}}\|_{L^\infty(\partial\Omega_c^N)}^2 \left(\|u^{\mathrm{DC}}\|_{L^\infty(\partial\Omega_c^N)} + \|u^{\mathrm{AC}}\|_{L^\infty(\partial\Omega_c^N)}\right)\right),
\end{aligned} \tag{A7}$$

where C depends on the size of Ω_c and $\partial\Omega_c^N$.

$R_{\hat{p}}$ term

Finally, by applying similar steps and noting that $\nabla \times \boldsymbol{A}^{\mathrm{AC}} = \mu_0 \boldsymbol{H}^{\mathrm{AC}}$ in $\mathrm{supp}(\boldsymbol{J}^{\mathrm{AC}})$ we have

$$
\begin{aligned}
|R_{\hat{p}}(t)| &\leq ||\nabla \times \boldsymbol{A}^{\mathrm{AC}}||_{L^2(\mathrm{supp}(\boldsymbol{J}^{\mathrm{AC}}))} ||\boldsymbol{J}^{\mathrm{AC}}||_{L^2(\mathrm{supp}(\boldsymbol{J}^{\mathrm{AC}}))} \left(||\nabla \hat{p}^{\mathrm{DC}}||_{L^2(\mathrm{supp}(\boldsymbol{J}^{\mathrm{AC}}))} + ||\nabla \hat{p}^{\mathrm{AC}}||_{L^2(\mathrm{supp}(\boldsymbol{J}^{\mathrm{AC}}))} \right) \\
&\leq \mu_0 ||\boldsymbol{H}^{\mathrm{AC}}||_{L^2(\mathrm{supp}(\boldsymbol{J}^{\mathrm{AC}}))} ||\boldsymbol{J}^{\mathrm{AC}}||_{L^2(\mathrm{supp}(\boldsymbol{J}^{\mathrm{AC}}))} \left(||\nabla \hat{p}^{\mathrm{DC}}||_{L^2(\mathrm{supp}(\boldsymbol{J}^{\mathrm{AC}}))} + ||\nabla \hat{p}^{\mathrm{AC}}||_{L^2(\mathrm{supp}(\boldsymbol{J}^{\mathrm{AC}}))} \right) \\
&\leq C\mu_0 ||\boldsymbol{H}^{\mathrm{AC}}||_{L^\infty(\mathrm{supp}(\boldsymbol{J}^{\mathrm{AC}}))} ||\boldsymbol{J}^{\mathrm{AC}}||_{L^\infty(\mathrm{supp}(\boldsymbol{J}^{\mathrm{AC}}))} \left(||\nabla \hat{p}^{\mathrm{DC}}||_{L^\infty(\mathrm{supp}(\boldsymbol{J}^{\mathrm{AC}}))} + ||\nabla \hat{p}^{\mathrm{AC}}||_{L^\infty(\mathrm{supp}(\boldsymbol{J}^{\mathrm{AC}}))} \right),
\end{aligned}
\tag{A8}
$$

where C depends on the size of the gradient coils $\mathrm{supp}(\boldsymbol{J}^{\mathrm{AC}})$.